

OPTIMIZATION OF CHARGE COLLECTION EFFICIENCY IN MSM  
PHOTODETECTOR

---

A Thesis presented to the Faculty of Graduate School  
University of Missouri-Columbia

---

In Partial Fulfillment  
Of Requirements for the degree  
Master of Science

---

By

SRAVANTHI KACHE

Dr Naz. E. Islam, Thesis Supervisor

DECEMBER 2005

The undersigned, appointed by the Dean of the Graduate School,  
have examined the thesis

OPTIMIZATION OF CHARGE COLLECTION EFFICIENCY IN MSM  
PHOTODETECTOR

Presentation by Sravanthi Kache

A candidate for the degree of Master of Science

And hereby certify that in their opinion it is worthy of acceptance

Nazh

---

Robert W. McLaren

---

HR - Chakrabarti

---

## **ACKNOWLEDGEMENTS**

I would like to thank everyone who encouraged me during my Masters. This thesis could not have been written without the guidance of my advisor Dr Naz E Islam who not only encouraged me during my research work but also challenged me through out my academic program. I would also like to thank Dr Mc Robert Laren and Dr H.R Chandrashekar for readily accepting to be in my thesis examining committee. Also I would like to especially like to thank Dr Kirawanich Phumin for encouraging me during my research project and exchanging valuable ideas during my thesis writing.

I would like to thank my parents and all my family members for encouraging me to pursue Masters and supporting me through out my education. I would especially like to thank my uncle Ajit Kache for being constant source of inspiration and always showed me the best way to approach any situation. In the end I would like to thank all my friends and colleagues for encouraging me through out my thesis writing.

I dedicate my thesis to my uncle Ajit Kache.

# TABLE OF CONTENTS

<b>ACKNOWLEDGMENTS.....</b>	<b>ii</b>
<b>LIST OF FIGURES.....</b>	<b>v</b>
<b>NOMENCLATURE.....</b>	<b>vii</b>
<b>CHAPTER 1 INTRODUCTION.....</b>	<b>1</b>
1.1 Introduction.....	1
<b>CHAPTER 2 LITERATURE REVIEW.....</b>	<b>6</b>
2.1 Photodetectors.....	6
<b>CHAPTER 3 THEORITICAL BACKGROUND.....</b>	<b>14</b>
3.1 Photodetector.....	14
3.1.1 Rise time and Bandwidth of a Photodetector.....	16
3.1.2 Compatibility of a Photodetector with Optical Communication System.....	17
3.1.3 MSM Photodetectors.....	19
3.2 Electromagnetic Waves.....	22
3.2.1 Maxwell's Equations.....	22
3.2.2 Propagation of Electromagnetic Waves.....	25
3.2.3 Reflection and Transmission of Electromagnetic Waves.....	26
3.2.3.1 Normal Incidence on a Lossless Dielectric.....	26
3.2.3.2 Oblique Incidence at a Dielectric Boundary.....	31
3.2.4 Energy Transported by EM waves.....	37
3.3 Simulation Software.....	39
3.3.1 Numerical Techniques Used.....	40
3.3.1.1 FDTD Technique.....	40
3.3.1.2 EFIE Technique.....	41
3.3.1.3 FIT Technique.....	41
3.3.2 CST Microwave Studio.....	41
3.3.3 Key features of different solver types.....	43
3.3.3.1 Transient solver.....	43
3.3.3.2 Eigen-Mode solver.....	44
3.3.3.3 Modal Analysis solver.....	44

3.3.3.4	Frequency Domain solver .....	45
3.3.4	Visualization and Secondary Results Calculation .....	45
<b>CHAPTER 4</b>	<b>OPTIMIZATION OF THE PERFORMANCE OF PHOTODETECTOR .....</b>	<b>47</b>
4.1	Introduction.....	47
4.2	Comparison between Different Structures.....	55
4.3	Optimization by varying the height of gratings .....	58
4.4	Optimization by Varying the Number of Gratings on the Active Region .....	62
4.5	Optimization of Charge Collection Efficiency by Using a Cladding of SiO <sub>2</sub> .....	64
<b>CHAPTER 5</b>	<b>CONCLUSION AND FUTURE WORK.....</b>	<b>71</b>
<b>REFERENCES</b>	<b>.....</b>	<b>75</b>

## LIST OF FIGURES

Figure 1: Schematic view of a band-gap diagram of a photodetector .....	15
Figure 2 MSM Photodetector.....	20
Figure 3 Spatial variation of E and H fields for an EM wave traveling in Z-direction ....	24
Figure 4 Uniform plane wave normally incident on a lossless dielectric boundary .....	27
Figure 5 A perpendicularly polarized wave incident on a dielectric boundary .....	33
Figure 6 A parallel polarized wave incident on a dielectric boundary .....	36
Figure 7 Single wall grating used on the active region used for analysis.....	53
Figure 8 Input Excitation Signal (continuous sine wave).....	56
Figure 9 Configuration of MSM photodetectors used in simulation. Structures are a 10×10×2 μm Si-substrates (a) without gratings (b) square gratings (c) cone gratings (d) hatched gratings.....	56
Figure 10 (a) Bulk Si photodetector with different 1.8-μm tall grating structures i.e square, cone and hatched cone (b) isoline plot of incident wave transmitted through substrate, square, cone and hatched cone structures. The curves display the optimum height, $h_{op}$ of each structure .....	57
Figure 11 Top view of a contour plot of the incident wave transmitted through the substrate: square, cone, and hatched cone structures.....	58
Figure 12 Incident wave amplitude change for a square grating with the grating height varying from 0.5μm to 1.3μm.....	59
Figure 13 Incident wave amplitude change for a cone grating with the grating height varying from 0.5μm to 1.3μm.....	60
Figure 14 Incident wave amplitude change for a hatched cone grating with the grating height varying from 0.5μm to 1.3μm.....	60
Figure 15 Normalized (with 1 V/m) E-field peak associated with a square (white), cone (gray), and hatched cone (black) structures as a function of height. ....	62
Figure 16 Relationship between the number of gratings and the normalized E-field peak associated with square (white), cone (gray), and hatched cone (black) structures as a function of height.....	63
Figure 17 Structure consists of a 10×10×2 μm Si substrate. The Si hatched cone gratings on top of the bulk Si are coated with a SiO <sub>2</sub> layer of thickness 0.1 μm.....	64
Figure 18 Waveforms of E-fields of the structure consisting of hatched cone Si and SiO <sub>2</sub> coating with different heights (+: 0.5μm, line: 0.6μm, and *: 0.7μm) .....	65
Figure 19 Structure consists of a 10×10×2 μm Si substrate. The Si square gratings on top of the bulk Si are coated with SiO <sub>2</sub> layer of thickness 0.1μm.....	65
Figure 20 Waveforms of E-fields of the structure consisting of square Si and an SiO <sub>2</sub> coating with different heights (+: 0.5μm, line: 0.6μm, and *: 0.7μm) .....	66
Figure 21 Structure consists of a 10×10×2 μm Si substrate. The Si cone gratings on top of the bulk Si are coated with SiO <sub>2</sub> gratings on top of the bulk Si are coated with SiO <sub>2</sub> layer of thickness 0.1μm.....	67
Figure 22 Waveforms of E-fields of the structure consisting of cone Si and SiO <sub>2</sub> coating with different heights (+: 0.5μm, line: 0.6μm, and *: 0.7μm).....	67

Figure 23 Structure consists of a $10 \times 10 \times 4 \mu\text{m}$ Si substrate with a bulk cladding layer of SiO <sub>2</sub> added on top of Si layer with a dimension of $10 \times 10 \times 3 \mu\text{m}$ . The Si hatched cone gratings on top of the bulk SiO <sub>2</sub> are coated with a SiO <sub>2</sub> layer of thicknesses $0.1 \mu\text{m}$ .....	68
Figure 24 Waveforms of E-fields of the structure consisting of hatched cone Si and SiO <sub>2</sub> coating and a bulk cladding layer on the substrate with different heights (+: $0.5 \mu\text{m}$ , line: $0.6 \mu\text{m}$ , and *: $0.7 \mu\text{m}$ ). .....	69

## NOMENCLATURE

Symbol	Physical Quantity	Unit
$\psi$	Electrostatic Potential	Volt, V
$q$	Electron charge	Coulomb, C
$c$	Speed of light	Meters per sec, M/s
$k$	Propagation constant/wave number	Radian per meter, rad/m
$\lambda$	Wave length	Meter, m
$f$	Frequency	Hertz, Hz
$E$	Electric Field Intensity	Volts per meter, V/m
$H$	Magnetic Field Intensity	Volts per meter, V/m
$D$	Electric Flux Density	Coulomb per square meter, C/m
$B$	Magnetic flux	Tesla, T
$\mu$	Permeability	Henry per meter, H/m
$\epsilon$	Permittivity	Farad per meter, F/m
$J_c$	Current Density	Ampere per square meter, A/m <sup>2</sup>
$\rho_v$	Volume charge density	Coulomb per cubic meter, C/m <sup>3</sup>
$S$	Poynting Vector	Weber per square meter, W/m <sup>2</sup>

$S_{av}$	Power Density	Weber per square meter, W/m <sup>2</sup>
$\sigma$	Conductivity	Siemens per meter, S/m
$\eta$	Intrinsic Impedance	Ohm, $\Omega$
$\omega$	Angular Frequency	Radians per second, rad/s
N	Refractive Index	-----
$\Gamma$	Reflection Coefficient	-----
$\tau$	Transmission coefficient	-----
Z	Characteristic Impedance	Ohm, $\Omega$
$\theta_i$	Angle of Incidence	Electrical Degrees, $^\circ$
$\theta_r$	Angle of Reflection	Electrical Degrees, $^\circ$
$\theta_t$	Angle of Transmission	Electrical Degrees, $^\circ$
$h$	Plank's Constant	-----
$E_g$	Bandgap energy	Electron Volts, eV
$\alpha$	Absorption Coefficient	-----
$\tau_{tr}$	Transit Time	Seconds, secs
$\tau_{RC}$	Time constant	Seconds, secs
$\Delta f$	Bandwidth	Kilobits per second, kbps or Kb/s
R	Responsivity	Amperes per watt, A/W

# Chapter 1 INTRODUCTION

## 1.1 Introduction

The research described in this thesis deals with a class of devices called photodetectors, which are used in optoelectronics and communication; specifically, it describes an effort to improve the charge collection efficiency of a detector made from Silicon (Si). Improving the charge collection efficiency would make the detector competent with GaAs in terms of speed, with the added advantage of making the detector compatible with available fabrication processes.

The birth of the photodetector can be dated back to 1873 when W.Smith discovered photoconductivity in selenium [33]. The progress of photodetectors was slow until Einstein explained the newly observed photoelectric effect in metals, and Planck solved the black body emission puzzle by introducing the quanta hypothesis. Applications such as temperature measurement, object detection, data retrieval, optical fiber communication and the like soon flourished after that.

Photodetectors used in telecommunications and optoelectronics are generally designed with a balance of bandwidth, efficiency and power-handling considerations. The reason is that these attributes are usually not mutually compatible; for example, small devices designed for ultra-high speed operation tend to exhibit low efficiency and/or a low power-handling capability. Photodetectors are basically semiconductor devices that absorb optical energy (light) and convert it into electrical energy, which is usually

manifested as photocurrent. High-speed and high-sensitivity photodetectors have been studied extensively over the past ten years owing to their application in broadband optical communication networks and optical generation of high power microwaves.

Photodetectors are an important part of optical communication systems. The design of the photodetector should be compatible with the remainder of the system, which requires that the photodetector should have a small size, a low bias voltage and should be easy to integrate into the receiver system.

The performance of the photodetector depends on the flux and distribution of light intensity within the structure under examination as well as on the material and electronic parameters, such as band structures and doping levels. Depending on the application, the performance refers to sensitivity, short response times, wavelength selectivity and other characteristics. To optimize the performance of the detector element, one can influence the light intensity distribution within, which, in turn, depends on the geometric and optical parameters of the structure as well as on the properties of the incident radiation. Computer simulations can significantly speed-up the design process. If such simulations are to provide useful information, however, the simulations need to take into account all important of the factors that influence the device performance.

There exists a large variety of photodetectors. To choose a photodetector for a specific application, the first criteria are the applicable range of wavelengths, the speed responsivity and the cost. Among the most frequently used photodetectors the MSM photodetector is class of detectors known as the metal-semiconductor-metal (MSM) structures, which have attracted a great deal of attention in recent years. A conventional

MSM consists essentially of two back-to-back Schottky contacts deposited over an undoped substrate. They offer good electrical bandwidth, low dark current and are easy to fabricate. One of the major problems faced by MSM photodetectors is that the interdigitated metal surface of the fingers on the semiconductor reflects light and hence a large portion of the incident photons is lost. The MSM photodetector has a major advantage in its high speed and its compatibility with FET technology. Its simple planar structure is easy to integrate with FETs in a single chip. One potential application is an integrated receiver for fiber optic communication

In the past few years, MSM photodetectors (PDs) became very popular in the field of optical communications because of their numerous advantages. One of the most important advantageous properties is its high response speed, which is determined by the geometry of the structure and by the low capacitance of the detector. The basic aim of further development of the MSM PDs is to achieve an improvement of antecedent properties. There is therefore an increasing interest in the modeling of MSM PD's and computer simulations of their response. Computer simulation is a better alternative to the fabrication and testing of a structure with or having only minor changes in the material properties or geometry.

In this research an Si MSM photodetector was modeled using an electromagnetic simulation software code called CST microwave software. The objective is to minimize the reflections and maximize the absorption by efficient light trapping in the active region. This will increase the efficiency of the MSM photodetector. One way to achieve higher efficiency is by using Si gratings on top of the substrate. In this project the focus is

on the charge collection efficiency of the device by studying the electromagnetic field analysis of the transmitted electromagnetic field components through the Si grating structure. A sinusoidal wave with energy above the band gap energy of Si was used as the excitation signal.

In this thesis the EM field transport process has been looked at further with a detailed analysis of the structure and geometry necessary for maximum energy absorption in the active region. In particular there is an attempt to optimize the collection efficiency by optimizing the grating shape, and height and the area covered by the gratings on the active region. The variations in the amplitude of the transmitted electric field intensity in the photodetector were determined for different cases in order to ensure the maximum possible collection efficiency. Finally, this thesis also analyzes the effects of the coating over these grating structures to determine the resulting variations in the electric field in the substrate (active region).

This thesis consists of six chapters. This introduction is followed by a literature review, where a brief history of the research in this area is presented.

The third chapter provides a detailed discussion of the physics of photodetectors and MSM photodetectors. It discusses all of the important parameters used in the design of PDs and the main functions of the PDs. It also discusses the advantages and the disadvantages of PDs and MSM PDs. Chapter 3 also discusses the reflection and transmission of the EM waves between two media, together with equations related to the efficiency of EM waves for the case of normal and oblique incidence being presented in detail. Chapter 3 also discusses the different numerical methods used to solve

electromagnetic problems. It also describes the CST Microwave software as the simulation tool, is the focus of the research to be presented here.

Chapter 4 presents the results and analysis of the various models used to improve the charge collection efficiency of the device. It discusses the various parameters that can be changed in order to improve the efficiency. For example, a change in the area covered by the gratings on the active region leads to improved charge collection efficiency. Simulation results for each case of a variation in the size and shape of the grating are also presented and discussed.

Chapter 6 concludes the thesis with a summary of the project and presents new ideas which could be pursued for further research in this area.

## Chapter 2 LITERATURE REVIEW

### 2.1 Photodetectors

Since its inception in the optoelectronics and communications industries, photodetectors have been extensively studied and researched both at the academia and industry levels. Most of the research has been focused on the optical to electrical conversion process. The photodetector is a key component in optical communication systems. The basic parameters used to characterize a photodetector are responsivity, quantum efficiency; rise time and bandwidth, this requirement being especially important as systems become faster. There is a need and motivation to improve the parameters.

The two major trends in PD development are aimed at developing a large bandwidth-efficiency product and a high saturation current. A paper by K.Kato et al [1] first outlines these trends and their limiting factors. They then discuss several PD technologies based on the waveguide photodiode (WGPD) for these two trends. Finally, they present a recently developed WGPD-based 50 Gb/s receiver optoelectronic integrated circuit (OEIC) technology.

R.G. DeCorby et al [2] discuss how photodetectors are generally designed with a balance of bandwidth, efficiency, and power handling capabilities that are then to be used in telecommunications and optoelectronics. This has been done by using the technique of coherent summation of photocurrent in a broadband, impedance-matched MSM photodetector array in order to relax bandwidth/power handling limitations.

An ultra-fast photoconductive switch was proposed by J.F.Holzman et al [3]; the geometry of the switch allows an ultra-short pulse to turn on and off the switch. The model employed here describes the photoexcitation of both a microstrip photoconductive layout and a coplanar photoconductive switch layout; both are able to achieve sub-picosecond switching.

M.Carria et al [4] have performed responsivity measurements on commercial silicon photodetectors in the UV range, 200–400 nm. In [4] microstrip and pixel detectors have been used; also, they have performed measurements in back illumination geometry which is of particular interest in most industrial applications. Promising results were obtained with commercial photodetectors in the UV range in terms of photocurrent stability and sensitivity, which opens up a variety of applications. M. Y. Liu [5] has proposed a metal-semiconductor-metal photodetector with 100-nm finger spacing and width on a silicon-on-insulator (SOI) substrate that has a scaled active layer, which were fabricated and characterized using electro-optic sampling. The key feature in speed enhancement is a buried oxide layer that limits the active Si thickness. A bandwidth of 140 GHz at a wavelength of 780nm was achieved by using this model. Good metal-semiconductor Schottky contact and low detector dark current have been achieved.

A new technique was proposed by Stephane Collin et al [6] for efficient light absorption in MSM photodetectors. It is shown that the confinement of light in sub-wavelength metal-semiconductor gratings can be achieved by Fabry-Perot resonances involving

vertical transverse magnetic and transverse electric guided waves, thereby increasing the quantum efficiency.

An increased interest in MSM photodetectors has developed over the past few years due to its low capacitance and high speed. Using these detectors an optical communication receiver has been fabricated with integrated circuits. A novel monolithic integrated optoelectronic (MSM photodetector) mixing receiver with low conversion loss is demonstrated by Qing.Z.Liu. [7]. This configuration of an OE mixer can be applied to a wideband sub-carrier multiplexed (SCM) distribution system to operate GHz range. Recently, an MSM detector has been utilized as an OE mixer in a frequency modulated continuous-wave laser detection and ranging (LADAR) system [8].

The response speed of an MSM photodetector is largely limited by the transit time of the photogenerated carriers, and thus, the inter-electrode spacing should be small. Finger width has been decreased down to the sub-micrometer and even nanometer scale as the fabrication technology advanced. MSM PD's with only 25nm finger width and spacing were fabricated using e-beam lithography. Y.Liu [9] has demonstrated an MSM photodetector with finger spacing smaller than the wavelength of the light. The transmission of TE and TM waves through the detector fingers becomes strongly dependent on the wavelength and polarization of the incident light.

Sang-Woo Seo et al [10] demonstrated a new kind of MSM photodetector called the "inverted metal semiconductor metal photodetector" which has higher efficiency. These are thin film MSMs without the growth substrate. IMSM's have fingers at the bottom of the device to enhance the efficiency.

At IR wavelengths, both silicon and GaAs are viable candidates for the fabrication of monolithically integrated optical receivers. On the other hand, silicon is a more attractive material than GaAs because of its low cost and potential for very large scale integration (VLSI), based on well established CMOS or bipolar technologies. GaAs gives large bandwidths and good responsivity. Si [11], [12] is not a very good photodetector material at high frequencies due to degraded bandwidth. A novel SIO photodetector is fabricated and quantitatively analyzed in [13]. This device exhibited extremely low dark currents, small capacitance, a large, dynamic range and no evidence of low frequency gains. Thus it is viable candidate for fiber-optic data links. [13]

Lee et al [14] have proposed an MSM detector configuration on a  $5\ \mu\text{m}$  thick Si membrane, where the trapping of light in a thin membrane results in a minimal reduction in responsivity, while reducing carrier transit times. Other attempts to improve the absorption of Si by hydrogenated amorphous Si (a-Si-H) have focused on modifying the long-range structural symmetry of crystalline Si by relaxing the k-selection rule for optical transition [15].

High sensitivity photodetectors are crucial for optical communications, information and sensing systems. A resonant cavity enhanced photodetector (RCE) provides wavelength selectivity in detection. These detectors can function as channel discriminators in wavelength division multiplexing systems. [16] This is achieved by utilizing reflectors around the active region. The photons make multiple passes across the active region, improving the probability of absorption, thereby increasing the quantum efficiency. A general expression for efficiency of RCE photodetectors was derived while taking the

external layer losses into account for the first time. Some attempts have been aimed at improving the Si MSM detector quantum efficiency at visible and near IR wavelengths by fabricating vertical and U-shaped trench electrodes using reactive ion etching and wet chemical etching methods. [17], [18].

For an MSM photodetector, the amount of energy reaching the interface of the detector should be a maximum, the amount of energy depends on the geometric and optical parameters of the structures as well as on the properties of the incident radiation (wavelength, polarization, angle of incidence, and the like). J.J. Kuta et al [19] demonstrated how polarization and wavelength account for the response of a MSM photodetector. For structures that are large compared to the wavelength, sufficiently good approximations can be obtained by means of simple geometric optics models. As feature sizes become smaller, the errors caused by neglecting diffraction and interference effects increase. When the feature sizes are below the order of a few wavelengths, rigorous electromagnetic models are necessary to obtain reasonably accurate results.

It [20] was found that approximately 30% of the incident light is reflected at the interface between the air and the detector surface. If one neglects the grating effect of fine metal fingers, these effects, in combination with occultation of possible absorbing surface area by metal electrodes of typically, at least 25% can reduce the overall quantum efficiency. An MSM photodetector with a submicron grating has been developed by Jinwook Burm et al, [20] for applications in monolithic integrated optical receiver circuits capable of detecting a millimeter wave modulation signal. A layer of  $Al_xGa_{1-x}As$  cap layer was grown to prevent any surface recombination of carriers and to minimize top surface

reflections. Using this layer design, millimeter-wave bandwidths were achieved without sacrificing the quantum efficiency.

A wave-guide photodetector based on amorphous silicon has been fabricated by Marta [21]. A computer solution technique was used to investigate the propagation characteristics of guided wave photodetectors arising from the interaction of light with silicon and metal cladding layers, and the overall absorption efficiency was calculated.

MSM photodetectors with finger spacing of  $\lambda$  small width were fabricated on bulk and at a low temperature grown GaAs and crystalline Si using ultra high resolution electron beam lithography by Stephen Y.Chou [22]. Montecarlo simulation was used to understand the impulse response of the MSM photodetector and to explore the ultimate speed limitation of transit- time-limited MSM PD's on GaAs and Si .Also a calculation to find the detector capacitance was done in that paper.

Optoelectronic integrated circuits are very promising for use in optical communication systems because of their high performance characteristics and small size. Circuit simulations of electronic circuits and photodetectors must be conducted for enhancing their performance. E.Sano [23] proposed an analytical model based on the behavior of photo-generated carriers and electric fields. This model was implemented on a SPICE-like circuit simulator and was found to be useful for designing high performance optoelectronic receivers. More simulation models have to be developed in order to improve the optical transmission characteristics.

In [24], A.K Sharma has demonstrated an improvement in quantum efficiency and frequency response at near-IR wavelengths of a NI-Si-Ni MSM photodetector. A simple

ion implantation was done on the photodetector, which created a highly absorbing region below the Si surface, thus improving the quantum efficiency. This device is CMOS compatible and can be readily integrated with conventional Si fabrication. Applications include AlGaAs diode laser local area networks operating at 860nm and mutichip module optical interconnections at  $1.06 \mu m$  .

A.K. Sharma and S.H.Zaidi [25] have demonstrated a Si MSM photodetector with improved efficiency and speed of the detector by using a sub-wavelength grating structure on the top of the active region. This top region serves as an anti-reflective coating reducing the Si reflectivity over a broad wavelength range and at the same time enhancing both the efficiency and speed of the device by coupling energy into higher diffraction orders that are absorbed closer to the Si surface. In that paper they have reported one-dimensional and two-dimensional grating structures. They demonstrated in [26] a model for reflection and transmission diffraction orders as a function of wavelength. They concluded that the energy and the angle of the transmitted diffraction higher-order modes as a function of the nanostructure geometry is the key mechanism that improved the device performance.

In [27] it is demonstrated that having structural changes at the interface leads to higher transmission energy and subsequent generation and collection of carriers at the surface. Variations in the electric field intensity due to a change in the number and dimension of square gratings were demonstrated.

A.K.Sharma and S.H.Zaidi have demonstrated Si MSM photodectors that use blaze, wall-like sub-wavelength gratings on the active region of the device. They tried improving the

efficiency and speed of the detector by using these gratings. This thesis is an extension of their work that will use computer simulation software (CST Microwave software). An MSM photodetector was designed to optimize the charge collection efficiency of the device by changing the shape, height and area covered by the gratings on the active region of the device. Finally, a coating of  $\text{SiO}_2$  was used over these gratings to observe the changes in the E-field on the substrate.

## Chapter 3 THEORITICAL BACKGROUND

This chapter discusses the basic physics and operation of a photodetector. It describes some of the important parameters related to the photodetector and its usage in optical communication systems. A detailed discussion of an MSM photodetector and its compatibility with optical systems is presented. Later in this chapter, a detailed discussion on the transmission through and the reflection from different materials of EM waves and the transmitted power through the material will be presented. Finally, this chapter discusses the simulation method used to model the device.

### 3.1 Photodetector

A basic photodetector consists of a semiconductor slab with ohmic contacts deposited on its two facets so that an external voltage can be applied across the slab as shown in Fig1. Light is incident on the slab of width 'W' from the top. If the energy,  $\hbar \nu$ , of the incident photons exceeds the band gap energy, an electron-hole pair is generated each time that a photon is absorbed by the semiconductor. That is,

$$\hbar \nu > E_g = \frac{1.24}{\lambda_c}$$

Where  $\hbar$  = plank's constant

$\nu$  = velocity of light

$E_g$  = band gap energy

$\lambda_c$  - cut off wavelength

Under the influence of the electric field created by the applied voltage, electrons and holes are swept across the semiconductor, resulting in a flow of electric current. The photocurrent  $I_p$  is directly proportional to the incident optical power  $P_{in}$ , that is,

$$I_p = R_d P_{in} \quad (3.1)$$

Where  $R_d$  is called the responsivity of the photodetector because more current is produced at a given input power for large value  $R_d$ .

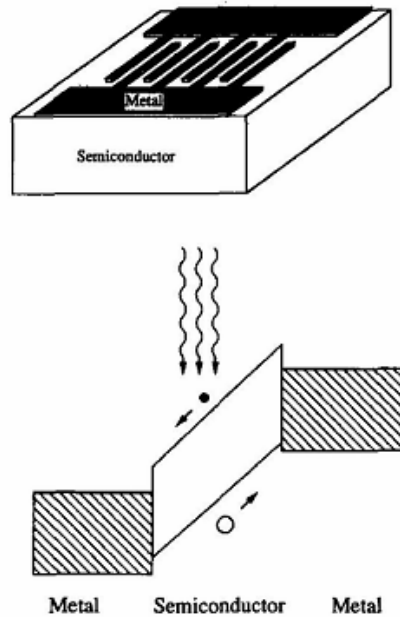


**Figure 1: Schematic view of a band-gap diagram of a photodetector**

The responsivity can be expressed in terms of the quantum efficiency,  $\eta$ , and can be defined as

$$R_d = \frac{\eta \lambda}{1.24} \quad (3.2)$$

where  $\lambda$  is the wavelength of the incident wave, and  $\eta$  is the quantum efficiency.

The responsivity of the photodetector increases as the wavelength increases simply because more photons are present for the same optical power. The dependence of the quantum efficiency  $\eta$  on  $\lambda$  is based on the absorption coefficient  $\alpha$ . If the facets of the semiconductor slab are assumed to have an antireflection coating, the power transmitted through the slab of width  $W$  is,

$$P_{tr} = e^{-\alpha W} P_{in} \quad (3.3)$$

Here,  $P_{tr}$  is the transmitted power,  $\alpha$  is the absorption coefficient,  $W$  is the slab width, and  $P_{in}$  the incident power.

The absorbed power can be written as

$$P_{abs} = (1 - e^{-\alpha W}) P_{in} \quad (3.4)$$

$$\eta = \frac{P_{abs}}{P_{in}} = 1 - e^{-\alpha W} \quad (3.5)$$

Here  $P_{abs}$  is the absorbed power.

### 3.1.1 Rise time and Bandwidth of a Photodetector

It is useful to introduce the concept of rise time  $T_r$ , defined as the time over which the current builds-up from 10% to 90% of its final value when the incident optical power is changed abruptly.  $T_r$  will depend on the time required for the electrons to travel to the electrical contacts. It will also depend on the response time of the electrical circuit used to process the photocurrent.

The rise time of the photodetector can be written by extending the rise time for the RC circuit (where  $R$  and  $C$  are the resistance and capacitance of the circuit) and is given by

$$T_r = 2.22(\tau_{RC} + \tau_{tr}) \quad (3.6)$$

Where  $\tau_{tr}$  is the transit time and  $\tau_{RC}$  is the time constant of the equivalent circuit. The transit time is included since time is required before the carriers are collected after their generation through absorption of photons. The maximum collection time is just equal to the time required for an electron to traverse the absorption region. Now,  $\tau_{tr}$  can be reduced by decreasing  $W$ , but that would reduce the quantum efficiency as well.

The bandwidth of the photodetector is determined by the speed with which it responds to variations in the incident optical power. The bandwidth of the photodetector is defined as

$$\Delta f = [2\pi(\tau_{RC} + \tau_{tr})]^{-1} \quad (3.7)$$

Where  $\tau_{tr}$  is the transit time,  $\tau_{RC}$  is the time constant of the equivalent circuit, and  $\Delta f$  is the bandwidth of the photodetector.

Along with the bandwidth and responsivity, the dark current,  $I_d$ , is also an important parameter. Here,  $I_d$  is generated in a photodetector in the absence of any optical signal and originates from stray light or from thermally generated electron-hole pairs. Dark current should be negligible for a good photodetector.

### 3.1.2 Compatibility of a Photodetector with Optical Communication System

A photodetector must satisfy very stringent requirements in performance and compatibility with optical communication systems when the conversion of an optical signal to an electrical signal is required. The main performance criteria for a good photodetector are:

1. High sensitivity at the operating wavelengths

2. High fidelity
3. Large optical to electrical conversion efficiency
4. High response speed
5. Large SNR at the output
6. High reliability and
7. Low sensitivity in performance to ambient conditions

The design of the photodetector should be compatible with the design and architecture of the remainder of the system; or also, since it is only one part of an entire optoelectronic system. Compatibility requires that the detector should have small-size, a low bias voltage and can be easily integrated into the receiver system.

*Terms Associated with Photodetectors:*

- Quantum Efficiency: The quantum efficiency of a photodetector is defined as the ratio of the electron generation rate to the photon incidence rate.
- Bandwidth: the bandwidth of a photodetector is determined by the speed with which it responds to variations in the incident optical power.
- Responsivity: In a photodetector, responsivity is the ratio of the electrical output to the optical input. Responsivity is usually expressed in amperes per watt, or volts per watt, of incident radiant power. Responsivity is a function of the wavelength of the incident radiation and the bandgap of the material of which the photodetector is made.

- Dark Currents: Dark currents are the currents generated in the detectors in the absence of any input optical signal and originate from stray light or from thermally generated electron-hole pairs. It is denoted by  $I_d$ .

### 3.1.3 MSM Photodetectors

A Metal Semiconductor Metal photodetector was proposed by Slavman and Figueroa and by Wei et al in 1981[28]. The concept of adding a thin barrier-enhancement layer to reduce the dark current was introduced in 1988 and has received much an interest, especially for high speed optical-fiber communication applications. MSM photodetectors have a simple device technology, fast response, small capacitance and a large active area. An MSM photodetector known as a Metal Semiconductor Metal Photodetector consists of a semi conducting absorbing layer sandwiched between two metal electrodes as shown in the Fig.2. As a result, a Schottky barrier is formed at each metal semiconductor interface, which prevents the flow of electrons from the metal to the semiconductor. Electron-hole pairs are generated through the absorption of light and flow towards the metal contacts, resulting in a photocurrent that is a measure of incident optical power. Light is received at the gap between the two metal contacts, and the MSM photodetector avoids absorption of light by the metal layer as in a conventional Schottky-barrier photodiode. For compound semiconductors, the light absorption layer is usually deposited on a semi-insulating substrate.

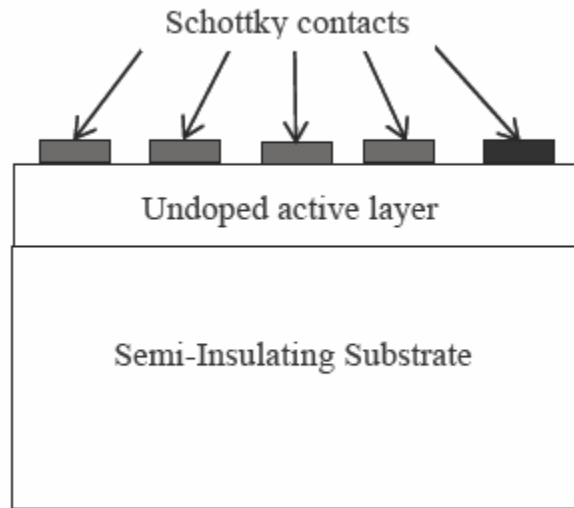


**Figure 2 MSM Photodetector**

An MSM photodetector has many advantages over other photodetectors. They have high speed and are highly compatible with FET technology. MSM photodetectors are inherently planar, which makes them easy to fabricate and compatible with the existing FET single pins. Due to their low capacitance and low dark currents (currents produced without any incident light), they can attain high speeds. However, the responsivity is very low compared to p-i-n photodiodes. The main causes for low responsivity is from the metal surface and the semiconductor surface, the finite carrier lifetime as the carriers traverse the gap between the electrodes before being collected, absorption of incident light outside the region in which the photogenerated carries can be collected by the electrodes, and surface recombination currents and deep traps within the semiconductor material, which may lower the detected optical signal.

MSM photodiodes have a much lower capacitance, which eliminates any parasitic capacitive coupling between the photodiode and the doped regions (per unit area) than p-i-n photodiodes and thus are often transit-time limited. The transit time is related to the spacing between the interdigitated electrodes. An MSM photodiodes can be used to improve the feasibility of fabricating optoelectronic integrated circuits for a fiber optic communication system because of its simple and compatible fabrication process. The integrability of the MSM photodiodes into with preamplifier circuitry comes from the fact that,

- I. MSM photodiodes do not require doping, which eliminates any parasitic capacitive coupling between the photodiode and the doped regions within the active transistors and,
- II. The Schottky electrodes of MSM photodiodes are essentially identical to the gate metallization of field effect transistors.

MSM photodiodes suffer from very low external quantum efficiency because the metallization for the electrodes shadows the active light- collecting region. Shadowing can limit the incident light from reaching the active region of the MSM detector and prevents the quantum efficiency from being more than 50% for equal electrode widths and spacing. There are design trade-offs in MSM photodiodes for optimizing speed and quantum efficiency. The average carrier transit time in an MSM photodiode can be decreased by reducing the absorption layer thickness, increasing the applied bias or reducing the interdigitated spacing. However a decrease in the absorption layer thickness results in degradation in responsivity; a decrease in electrode spacing leads to degradation

of the dark current and the break down voltage and the equipment for complex lithography.

### 3.2 Electromagnetic Waves

The analysis of energy transport through MSM photodetectors can be done through semiconductor or electromagnetic wave transmission analysis. Metal-Semiconductor-Metal (MSM) photodetectors operate on the same principle as *p-i-n* photodetectors. Their response is related to the current caused by the electron-hole pairs separated by the electric field in the depletion region of two Schottky diodes. In this thesis we analyzed a MSM photodetector has been analyzed through an electromagnetic approach using CST Microwave software as a simulation tool. The transmission of an electromagnetic wave through the photodetector and its amplitude changes while transmission through the photodetector will be analyzed.

#### 3.2.1 Maxwell's Equations

All classical electromagnetic phenomena are governed by a compact and elegant set of fundamental rules known as Maxwell's equations. They are based on a set of postulates by J.C.Maxwell in order to encompass the earlier experimentally derived laws of Faraday and Ampere. The four-coupled partial differential equations shown below were put forth as complete classical Maxwell's equations. They are used in designing antennas, transmission lines, cavity resonators, fiber optics and in solving radiation problems.

Maxwell's wave equations;

$$\Delta \times E = -\mu \frac{\partial H}{\partial t} \quad (3.7)$$

$$\Delta \times H = J_c + \varepsilon \frac{\partial E}{\partial t} \quad (3.8)$$

$$\Delta \cdot D = \rho_v \quad (3.9)$$

$$\Delta \cdot B = 0 \quad (3.10)$$

E= Electric field (V/m)

$\mu$  = Permeability (H / m)

H = magnetic field intensity (A/m)

$\epsilon$  =permittivity (F / m)

D= Electric flux Density ( C / m<sup>2</sup> )

$J_c$  =current density ( A / m<sup>2</sup> )

B= Magnetic flux density

$\rho_v$  =Volume charge density C / m<sup>3</sup>

In free space or a dielectric, Eqs 3.8 and 3.9 become

$$\nabla \times H = \epsilon \frac{\partial E}{\partial t} \quad (3.11)$$

$$\nabla \times D = \nabla \cdot E = 0 \quad (3.12)$$

By taking the curl of Equation 3.7 and substituting into Equation 3.11

$$\nabla \times (\nabla \times E) = -\mu \left[ \nabla \times \frac{\partial H}{\partial t} \right] = -\mu \epsilon \frac{\partial^2 E}{\partial t^2} \quad (3.13)$$

$$\nabla \times (\nabla \times E) = \nabla (\nabla \cdot E) - \nabla^2 E \quad (3.14)$$

$$\nabla \times (\nabla \times E) = \nabla (\nabla \cdot E) - \nabla^2 E = -\mu \epsilon \frac{\partial^2 E}{\partial t^2} \quad (3.15)$$

then,

$$\nabla^2 E = \mu \epsilon \frac{\partial^2 E}{\partial t^2} \quad V / m^3 \quad (3.16)$$

When expanded in Cartesian coordinates, Equation 3.16 becomes,

$$\frac{\partial^2 E}{\partial x^2} + \frac{\partial^2 E}{\partial y^2} + \frac{\partial^2 E}{\partial z^2} = \mu \epsilon \frac{\partial^2 E}{\partial t^2} \quad V / m^3 \quad (3.17)$$

The above equation is called the Maxwell's EM wave equation. All EM waves have to obey this special wave equation that describes the time and space dependence of the electric field. In an isotropic and linear dielectric medium, the relative permittivity is the same in all directions and is independent of the electric field.

The electric field and the magnetic field are important concepts that can be used to mathematically describe the physical nature of electromagnetic waves such as light. The electric field vibrates transverse to the direction of the electromagnetic wave. The magnetic field vibrates in the direction transverse to the electric field. Figure 3 illustrates the behavior of an electromagnetic wave that is polarized along the x-axis and traveling in the z-direction. These two fields oscillate in a consistent manner so that the wave moves forward at a constant rate, the speed of light. Light is an electromagnetic wave with time varying electric and magnetic fields,  $E_x$  and  $B_y$  respectively, propagating in space in such a way that they are always perpendicular to each other. The direction of propagation of the wave is in the z-direction.

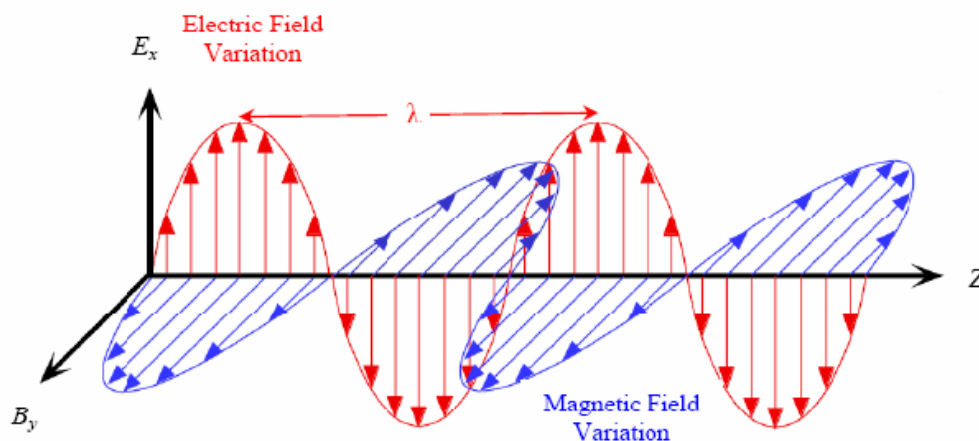


Figure 3 Spatial variation of E and H fields for an EM wave traveling in Z-direction

Electromagnetic (EM) waves are produced by moving charges, resulting in changing electric and magnetic fields carrying energy through space. EM waves require no medium; they can travel through empty space. Sinusoidal plane waves are one type of an electromagnetic wave. Not all EM waves are sinusoidal plane waves, but all EM waves can be viewed as a linear superposition of sinusoidal plane waves traveling in arbitrary directions. A plane EM wave traveling in the z-direction can be described by

$$E_x(z,t) = E_o \cos 2\pi(ft - z/\lambda) \quad (3.18)$$

Where  $E_x$  is the electric field at position z at time t,  $\lambda$  is the wavelength, f is the frequency and  $E_o$  is the amplitude of the wave. Time-varying magnetic fields result in time varying electric fields and vice versa. A time varying magnetic field would set up a time varying electric field with the same frequency.

### 3.2.2 Propagation of Electromagnetic Waves

Electromagnetic waves are waves that can travel through the vacuum of outer space. Mechanical waves, unlike electromagnetic waves, require the presence of a material medium in order to transport their energy from one location to another. Electromagnetic waves are created by the vibration of an electric charge. This vibration creates a wave which has both an electric and magnetic component. The propagation of an electromagnetic wave through a material medium occurs at a net speed which is less than  $3 \times 10^8 \text{ m/s}$ .

### 3.2.3 Reflection and Transmission of Electromagnetic Waves

#### 3.2.3.1 Normal Incidence on a Lossless Dielectric

When a uniform plane wave propagating in medium 1 is normally incident on an interface with a second medium with a different dielectric constant as shown in Fig 4, some of the incident wave energy is transmitted into medium 2 and continues to propagate to the right (+z direction). In the following discussion, it is assumed that both media are lossless dielectrics (i.e.  $\sigma_1, \sigma_2 = 0$ ). Once again, it is assumed that without loss of generality under conditions of normal incidence on a planar boundary, that the incident electric field is oriented in the x-direction. It is also assumed that the amplitude  $E_o^i$  of the incident wave is real, with no loss of generality, since this basically amounts to the choice of the time origin [29]. The phasor fields for the incident, reflected, and transmitted waves are given as:

Incident Wave:

$$E^i(z) = \hat{x}E_o^i e^{-jk_1 z} \tag{3.19}$$

$$H^i(z) = \hat{y} \frac{E_o^i}{\eta_1} e^{-jk_1 z}$$

Reflected Wave:

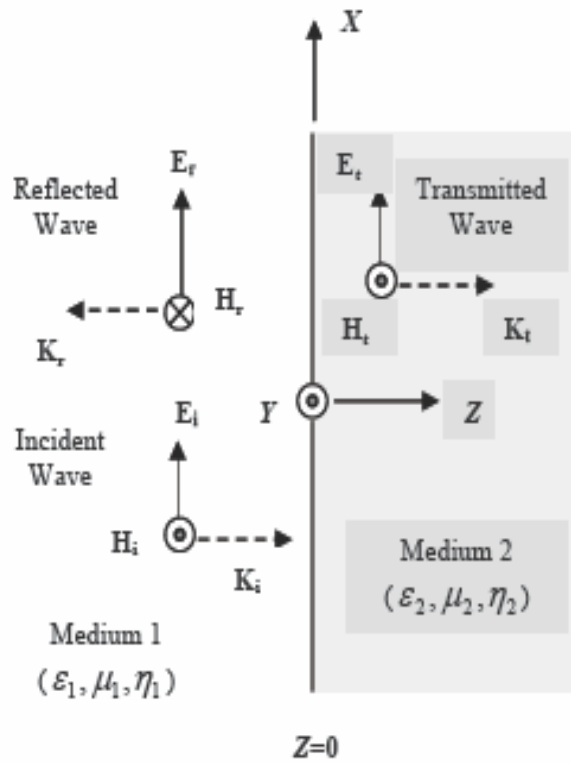


Figure 4 Uniform plane wave normally incident on a lossless dielectric boundary

$$E^r(z) = \hat{x}E_o^r e^{+jk_1z} \quad (3.20)$$

$$H^r(z) = -\hat{y} \frac{E_o^r}{\eta_1} e^{+jk_1z}$$

Transmitted Wave:

$$E^t(z) = \hat{x}E_o^t e^{-jk_2z} \quad (3.21)$$

$$H^t(z) = \hat{y} \frac{E_o^t}{\eta_2} e^{-jk_2 z}$$

Where,  $k_1 = \omega\sqrt{\mu_1\epsilon_1}$ ,  $k_2 = \omega\sqrt{\mu_2\epsilon_2}$  and  $\eta_1 = \sqrt{\mu_1/\epsilon_1}$ ,  $\eta_2 = \sqrt{\mu_2/\epsilon_2}$  are respectively, the wave number and the intrinsic impedance for medium 1 and 2, respectively. Note that  $E_o^t$  is the amplitude of the transmitted wave at  $z=0$ . From the Fig.4, the polarities of  $E^i$  and  $E^r$  have been defined to be the same and  $H^r$  is assumed to be in the  $-y$  direction, so that  $E^r \times H^r$  is in the  $-z$  direction. Note that, at this point, the selected orientations of E and H for the different waves (incident, reflected and transmitted) are simply convenient choices. The boundary conditions will determine whether the phasor fields at the boundary are positive or negative according to these assumed conventions.

Assuming that the incident wave is as shown, the next step is to determine the properties of the reflected and transmitted waves so that the fundamental boundary conditions for electromagnetic fields are satisfied at the interface, where all of the three waves are related to one another. There are two unknown quantities  $E_o^t$  and  $E_o^r$  to be determined in terms of the incident field amplitude  $E_o^i$ . Two boundary conditions will be used to determine them. The boundary conditions to be employed are 1) the tangential components of the electric field should be continuous across the boundary and 2) the tangential components of the magnetic field intensity differ by any surface current that is flowing located along the interface. It is reasonable in practice to assume that this current is equal to zero. This implies that the tangential components of the magnetic field

intensity will also be continuous at the interface. Thus, the two boundary conditions are continuity of the tangential components of both the electric and magnetic fields across the interface. We thus have

$$E^i(z=0) + E^r(z=0) = E^t(z=0) \Rightarrow E_o^i + E_o^r = E_o^t$$

$$H^i(z=0) + H^r(z=0) = H^t(z=0) \Rightarrow \left[ \frac{E_o^i}{\eta_1} \right] - \left[ \frac{E_o^r}{\eta_1} \right] = \left[ \frac{E_o^t}{\eta_2} \right]$$

The solution of these two equations yields

$$E_o^r = \frac{\eta_2 - \eta_1}{\eta_2 + \eta_1} E_o^i \quad (3.22)$$

$$E_o^t = \frac{2\eta_2}{\eta_2 + \eta_1} E_o^i \quad (3.23)$$

The reflection and transmission coefficients are defined as follows

$$\Gamma = \frac{E_o^r}{E_o^i} = \frac{\eta_1 - \eta_2}{\eta_1 + \eta_2} \quad (3.24)$$

$$\tau = \frac{E_o^t}{E_o^i} = \frac{2\eta_2}{\eta_2 + \eta_1} \quad (3.25)$$

The quantities  $\Gamma$  and  $\tau$  are called the Reflection Coefficient and Transmission Coefficient, respectively. For lossless dielectric media,  $\eta_1$  and  $\eta_2$  are real quantities; consequently, both  $\Gamma$  and  $\tau$  are real. Note that, physically, the above coefficients are derived from the application of the boundary conditions, which are valid for all media in general. Complex reflection and transmission coefficients may result when  $\eta_1$  and/or  $\eta_2$  are complex (i.e., one or both of the media are lossy). This means that, in addition to the differences in amplitude, phase shifts are also introduced between the incident, reflected

and transmitted fields at the interface. From Eqs. (3.24) and (3.25), it can be easily shown that  $\Gamma$  and  $\tau$  are interrelated by the simple formula,

$$\tau = 1 + \Gamma \quad (3.26)$$

For nonmagnetic media,

$$\eta_1 = \frac{\eta_0}{\sqrt{\epsilon_{r_1}}}, \quad (3.27)$$

$$\eta_2 = \frac{\eta_0}{\sqrt{\epsilon_{r_2}}}$$

Where,  $\eta_0$  is the intrinsic impedance of free space, in which case Eqs. (3.24) and (3.25) may be written as.

$$\Gamma = \frac{\sqrt{\epsilon_{r_1}} - \sqrt{\epsilon_{r_2}}}{\sqrt{\epsilon_{r_1}} + \sqrt{\epsilon_{r_2}}}, \quad (3.28)$$

$$\tau = \frac{2\sqrt{\epsilon_{r_1}}}{\sqrt{\epsilon_{r_1}} + \sqrt{\epsilon_{r_2}}} \quad (3.29)$$

For most dielectrics and insulators, the magnetic permeability does not differ appreciably from the free space value. Hence,  $\mu_1 = \mu_2 = \mu_0$  and, since the characteristic impedance,  $Z = \sqrt{\mu/\epsilon}$ . Eqs (3.28) and (3.29) can be written as,

$$\Gamma = \frac{\sqrt{Z_2} - \sqrt{Z_1}}{\sqrt{Z_2} + \sqrt{Z_1}} \quad (3.30)$$

$$\tau = \frac{2\sqrt{Z_2}}{\sqrt{Z_2} + \sqrt{Z_1}} \quad (3.31)$$

Hence, knowing the characteristic impedance of the materials allows one to determine the propagation characteristics and amplitudes of the wave that is transmitted into the second material and of the wave that is reflected at the interface and propagates back into the first material. If the characteristic impedances on both sides of the interface are equal, all of the incident electromagnetic energy will be transmitted into region 2 and none will be reflected back into region 1. This is called matching the media, which has many practical applications.

### 3.2.3.2 Oblique Incidence at a Dielectric Boundary

For normal incidence, the reflection coefficient,  $\Gamma$  and the transmission coefficient,  $\tau$ , of a boundary between two different media are independent of the polarization of the incident wave, because the electric and magnetic fields of a normally incident plane wave are both always tangential to the boundary, regardless of the wave polarization. This is not the case for oblique incidence at an angle  $\theta_1 \neq 0$ . A wave with any specified polarization may be described as the superposition of two orthogonally polarized waves, one with its electric field parallel to the plane of incidence (parallel polarization) and another with its electric field perpendicular to the plane of incidence (perpendicular polarization). These two types of polarizations will now be briefly discussed in the following sections.

#### 3.2.3.2.1 Perpendicular Polarization

Expressions for the electric and magnetic field phasors of the incident, reflected, and refracted (transmitted) waves as shown in Fig.5 can be written as:

Incident wave:

$$E^i(x, z) = \hat{y}E_o^i e^{-jk_1(z \sin \theta_i + z \cos \theta_i)}$$

$$(3.32)$$

$$H^i(x, z) = \frac{E_o^i}{\eta_1} (-\hat{x} \cos \theta_i + \hat{z} \sin \theta_i) e^{-jk_1(z \sin \theta_i + z \cos \theta_i)}$$

Reflected wave:

$$E^r(x, z) = \hat{y}E_o^r e^{-jk_1(z \sin \theta_r - z \cos \theta_r)}$$

$$(3.33)$$

$$H^r(x, z) = \frac{E_o^r}{\eta_1} (\hat{x} \cos \theta_r + \hat{z} \sin \theta_r) e^{-jk_1(z \sin \theta_r - z \cos \theta_r)}$$

Transmitted wave:

$$E^t(x, z) = \hat{y}E_o^t e^{-jk_2(z \sin \theta_t + z \cos \theta_t)}$$

$$(3.34)$$

$$H^t(x, z) = \frac{E_o^t}{\eta_2} (-\hat{x} \cos \theta_t + \hat{z} \sin \theta_t) e^{-jk_2(z \sin \theta_t + z \cos \theta_t)}$$

where  $\theta_i$  = Angle of incidence,

$\theta_r$  = Angle of reflection,

$\theta_t$  = Angle of transmission

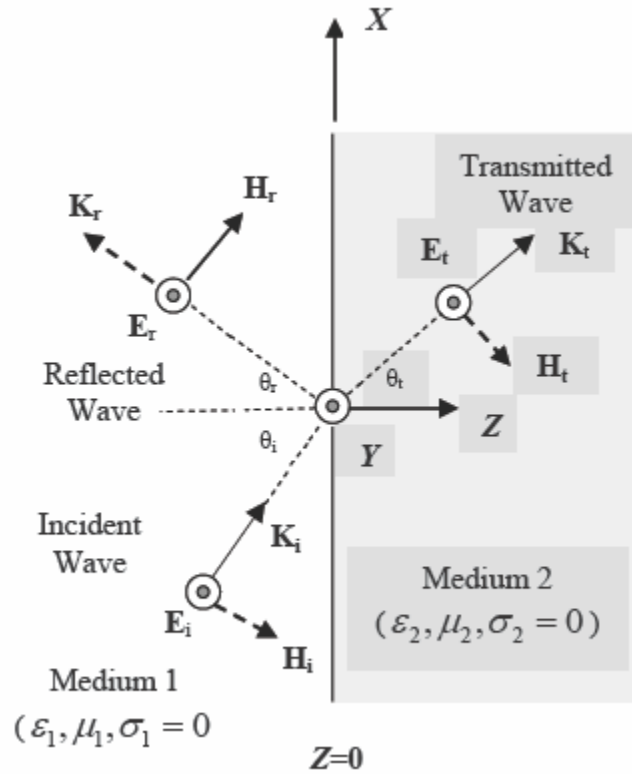


**Figure 5 A perpendicularly polarized wave incident on a dielectric boundary**

To determine the amplitudes of the reflected and transmitted wave fields in terms of the incident field amplitude  $E_o^i$ , one can apply the boundary condition requiring the continuity of the tangential component of the wave's electric field across the interface.

Considering the field orientations as shown in Fig 5, then at  $z=0$ ,

$$E_o^i e^{-jk_1 z \sin \theta_i} + E_o^r e^{-jk_1 z \sin \theta_r} = E_o^t e^{-jk_2 x \sin \theta_t} \quad (3.35)$$

Since this condition has to be satisfied for all values of  $x$ , all three components must be equal. Thus,0

$$k_1 x \sin \theta_i = k_1 x \sin \theta_r = k_2 x \sin \theta_t \quad (3.36)$$

The first equality in Eq (3.36) leads to

$$\theta_i = \theta_r \quad (3.37)$$

Eq (3.37) is commonly referred to as Snell's law. The second equality in Eq.(3.36) leads to

$$\frac{\sin \theta_i}{\sin \theta_t} = \frac{k_2}{k_1} = \frac{\omega \sqrt{\mu_2 \epsilon_2}}{\omega \sqrt{\mu_1 \epsilon_1}} = \frac{n_2}{n_1} \quad (3.38)$$

Eq. (3.38) is commonly referred to as Snell's law of refraction. Rewriting the boundary condition at any given value of x, (say at x=0),

$$E_o^i + E_o^r = E_o^t \Rightarrow \frac{E_o^t}{E_o^i} = 1 + \frac{E_o^r}{E_o^i} \quad (3.39)$$

On the basis of the conversation of power,

$$|S_{av}|_i \cos \theta_i = |S_{av}|_r \cos \theta_r + |S_{av}|_t \cos \theta_t \quad (3.40)$$

$$\frac{E_o^{r^2}}{E_o^{i^2}} = 1 - \frac{\eta_2 E_o^{t^2} \cos \theta_t}{\eta_1 E_o^{i^2} \cos \theta_i} \quad (3.41)$$

Now substituting Eq (3.39) into Eq (3.41) and manipulating the result to solve for  $\frac{E_o^r}{E_o^i}$

$$\Gamma_{\perp} = \frac{E_o^r}{E_o^i} = \frac{\eta_2 \cos \theta_1 - \eta_1 \cos \theta_1}{\eta_2 \cos \theta_1 + \eta_1 \cos \theta_1} \quad (3.42)$$

Where,  $\Gamma_{\perp}$  is called the reflection coefficient for perpendicular polarization. For magnetically identical media and using Eq (3.38), one can obtain an alternate expression for  $\Gamma_{\perp}$ .

$$\Gamma_{\perp} = \frac{E_0^r}{E_0^i} = \frac{\cos \theta_i - \sqrt{(\epsilon_{r_2}/\epsilon_{r_1}) - \sin^2 \theta_i}}{\cos \theta_i + \sqrt{(\epsilon_{r_2}/\epsilon_{r_1}) - \sin^2 \theta_i}} \quad (3.43)$$

The transmission coefficient  $\tau_{\perp}$  is given by,

$$\tau_{\perp} = \frac{2\eta_2 \cos \theta_i}{\eta_2 \cos \theta_i + \eta_1 \cos \theta_t} \quad (3.44)$$

For magnetically identical media,

$$\tau_{\perp} = \frac{2 \cos \theta_i}{\cos \theta_i + \sqrt{(\epsilon_{r_2}/\epsilon_{r_1}) - \sin^2 \theta_i}} \quad (3.45)$$

Hence,

$$\Gamma_{\perp} + 1 = \tau_{\perp} \quad (3.46)$$

### 3.2.3.2.2 Parallel Polarization

The expressions for the electric and magnetic field phasor of the incident, reflected and refracted (transmitted) waves as shown in Fig 6 can be written as

Incident Wave:

$$E^i(x, z) = E_o^i (\hat{x} \cos \theta_i - \hat{z} \sin \theta_i) e^{-jk_1(z \sin \theta_i + z \cos \theta_i)} \quad (3.47)$$

$$H^i(x, z) = \hat{y} \frac{E_o^i}{\eta_1} e^{-jk_1(z \sin \theta_i + z \cos \theta_i)}$$

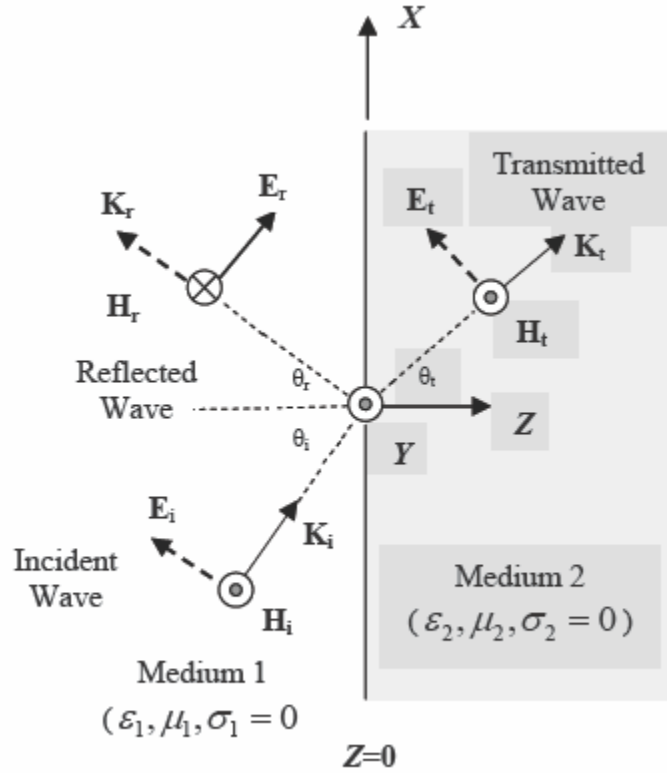


Figure 6 A parallel polarized wave incident on a dielectric boundary

Reflected wave:

$$E^r(x, z) = E_o^r (\hat{x} \cos \theta_r + \hat{z} \sin \theta_r) e^{-jk_1(z \sin \theta_r - z \cos \theta_r)} \quad (3.48)$$

$$H^r(x, z) = -\hat{y} \frac{E_o^r}{\eta_1} e^{-jk_1(z \sin \theta_r - z \cos \theta_r)}$$

Transmitted wave

$$E^t(x, z) = E_o^t (\hat{x} \cos \theta_t - \hat{z} \sin \theta_t) e^{-jk_2(z \sin \theta_t + z \cos \theta_t)} \quad (3.49)$$

$$H^t(x, z) = \hat{y} \frac{E_o^t}{\eta_2} e^{-jk_2(z \sin \theta_t + z \cos \theta_t)}$$

Following a procedure similar to that used for the perpendicular polarization case to find the amplitudes of the reflected and transmitted waves in terms of  $E_o^i$ , apply the boundary

condition requiring the continuity of the tangential component of the wave's electric field across the interface. Therefore, at  $z=0$ ,

$$(E_o^i + E_o^r) \cos \theta_i = E_o^t \cos \theta_t \quad (3.50)$$

Substituting Eq (3.50) into Eq (3.41) and manipulating the result to solve for  $E_o^r/E_o^i$ ,

$$\Gamma_{||} = E_o^r/E_o^i = \frac{-\eta_1 \cos \theta_i + \eta_2 \cos \theta_t}{\eta_1 \cos \theta_i + \eta_2 \cos \theta_t} \quad (3.51)$$

For magnetically identical media,

$$\Gamma_{||} = \frac{\cos \theta_t - \sqrt{(\epsilon_2/\epsilon_1) - \sin^2 \theta_i}}{\cos \theta_t + \sqrt{(\epsilon_2/\epsilon_1) - \sin^2 \theta_i}} \quad (3.52)$$

which is the reflection coefficient for parallel polarization,

For the transmission coefficient,

$$\tau_{||} = \frac{E_o^t}{E_o^i} = \frac{2\eta_2 \cos \theta_i}{\eta_1 \cos \theta_i + \eta_2 \cos \theta_t} \quad (3.53)$$

From Eqs 3.52 and 3.53,

$$\Gamma_{||} + 1 = \tau_{||} \left( \frac{\cos \theta_t}{\cos \theta_i} \right)$$

These wave propagation concepts can be applied for the analysis of an MSM photodetector as an EM wave incident on the gratings of the photodetectors reaches the active region.

### 3.2.4 Energy Transported by EM waves

Electromagnetic waves transport energy through space. In free space, this energy is transported by the wave with speed  $c$ . The magnitude of the energy flux,  $S$  is the amount

of energy that crosses a unit area perpendicular to the direction of propagation of the wave per unit time. It is given by

$$S = E \times H \quad (3.54)$$

Since, for electromagnetic waves,  $H=E/c$ ,

The Poynting vector is the energy flux vector. Its direction is that of the propagation of the wave, i.e. the direction in which the energy is transported.

$$S = E \times H \quad (3.55)$$

Energy per unit area per unit time is power per unit area.  $S$  represents the power per unit area in an electromagnetic wave. If an electromagnetic wave falls onto an area  $A$  where it is absorbed, then the power delivered to that area is

$$P = \int_A \langle S \rangle \cdot dA = S \cdot A \quad (3.56)$$

This concept of the transmission of energy can be applied for an MSM photodetector as the wave, after propagating through Si grating region, reaches the active region of the detector.

The mechanism of energy transport through a medium involves the absorption and reemission of wave energy by the atoms of the material. When an electromagnetic wave impinges upon the atoms of a material, the energy of that wave is absorbed. The absorption of energy causes the electrons within the atoms to undergo vibrations. After a short period of vibration motion, the vibrating electrons create a new electromagnetic wave with the same frequency as the first electromagnetic wave. While these vibrations occur for only a very short time, they delay the motion of the wave through the medium.

The actual speed of an electromagnetic wave through a material medium is dependent upon the optical density of that medium. When a light passes through a medium, its velocity decreases. For a given frequency of light, the wavelength also must decrease. This decrease in velocity is quantized by the refractive index, that is  $n$  of the medium, which is the ratio of  $c$  to the velocity of light in that medium  $v$ ,  $n = c/v$ . Since the velocity of light is less in media than in a vacuum,  $n$  is always a number greater than one. Different materials cause different amounts of delay due to the absorption and re-emission process.

Different materials have their atoms more closely packed and thus the distance between atoms is less. These two factors are dependent upon the nature of the material through which the electromagnetic wave is traveling. As a result, the speed of an electromagnetic wave is dependent upon the material through which it is traveling.

### 3.3 Simulation Software

#### **Introduction**

Various electromagnetic techniques have been used for solving complicated electromagnetic scattering problems. There are three major numerical techniques used, the Finite Difference Time Domain (FDTD), the Electrical Field Integral Equation method (EFIE), and the Finite Integration method (FIT). In all simulations in this thesis, the Finite Integration method has been used because it is capable of analyzing broadband structures, specifically in the high frequency range. These three techniques will be discussed briefly in the following sections.

CST Microwave studio is a powerful and easy to use electromagnetic and simulation software package. This program combines a user-friendly interface and simulation performance in an unsurpassed manner. With its native Windows based user interface, one can directly start with the electromagnetic problem presented here rather than dealing with a cryptic proprietary user interface. Excellent visual feedback at all stages of the simulation process allows one to achieve a very steep learning curve.

### 3.3.1 Numerical Techniques Used

#### 3.3.1.1 FDTD Technique

The FDTD technique is a computational method that calculates the temporal evolution of an electromagnetic field within a region of space by stepping through time. At each step, centered, finite-difference approximations are used to calculate the space and time differences on a Cartesian grid. The electric and magnetic fields are defined by six field components, which all lie on a different point on the grid, especially defined to fit into the FDTD scheme. This leads to an explicit time stepping algorithm which is of second order accuracy in both time and space. Calculation phases or terms can be divided into steady-state and transient analysis. The result is a function of time, which can be transformed into the frequency domain. [27]

The scattering of arbitrary-shaped perfectly conducting bodies is solved using a surface integral equation formulation for an electric field. The integral equation is solved by using the method of moments in which the testing functions of the electric field and the expansion functions of the electric surface current density are both appropriate triangular-

patch functions. The system of equations is then solved by using a LU factorization algorithm. The EFIE method is applicable to both open and closed surfaces.

### 3.3.1.2 EFIE Technique

The scattering of arbitrary-shaped perfectly conducting bodies is solved using a surface integral equation formulation for an electric field. The integral equation is solved by using the method of moments in which the testing functions of the electric field and the expansion functions of the electric surface current density are both appropriate triangular-patch functions. The system of equations is then solved by using a LU factorization algorithm. The EFIE method is applicable to both open and closed surfaces.

### 3.3.1.3 FIT Technique

Weiland first proposed this technique in 1976/77. It is a numerical method, which provides a universal spatial discretization scheme, and is applicable to various electromagnetic problems, ranging from static field calculations to high frequency applications in the time or frequency. In the following section, the main aspects of this procedure will explained and extended to specialized forms concerning the different solver types. The FIT method follows integral form of Maxwell's equations rather than the differential form as performed by most of the numerical methods [27]. This numerical technique is used in the simulation methods presented in this thesis

### 3.3.2 CST Microwave Studio

CST MICROWAVE SOFTWARE is a direct and iterative matrix solver with convergence acceleration techniques. It is a fully featured software package for electromagnetic analysis and design in the high frequency range. It simplifies the process of inputting the structure by providing a powerful solid modeling front-end, which is based on the ACIS modeling kernel. Strong graphic feedback simplifies the definition of your device even further. After a component has been modeled, a fully automatic meshing procedure is applied before the simulation engine is started.

The simulators feature the Perfect Boundary Approximation method and its Thin Sheet Technique extension, which increase the accuracy of the simulation by an order of magnitude in comparison to conventional simulators. Since no method works equally well in all application domains, the software contains four different simulation techniques which best fits for their particular application.

The different techniques available for simulation are

1. Transient Solver
2. Eigen mode Solver
3. Frequency domain Solver
4. Modal Analysis Solver

The most flexible tool from this list is the transient solver, which can generate the entire broadband frequency behavior of the simulated device from only one calculation run. This solver is very efficient for most kinds of high frequency applications, such as connectors, transmission lines, filters, antennas and many others. Efficient filter design often requires the direct calculation of the operating modes in the filter rather than an S-

parameter simulation. For these cases, the CST MICROWAVE STUDIO also features an Eigenmode solver, which efficiently calculates a finite number of modes in closed electromagnetic devices. This CST MICROWAVE STUDIO also contains modal-analysis solver, which works in combination with the Eigen mode solver. The transient solver becomes less efficient for low frequency problems, in which the structure is much smaller than the shortest wavelength. In these cases it can be advantageous to solve the problem by using the frequency domain solver. This approach is the most efficient when a few frequency points are of interest.

### 3.3.3 Key features of different solver types

#### 3.3.3.1 Transient solver

- Efficient calculation for loss-free and lossy structures
- Broadband calculation of S-parameter from one single calculation run by applying DFT's to time signals
- Calculations of field distributions as functions of time or at multiple selected frequencies from one simulation run.
- Adaptive mesh refinement in 3-D
- Plane wave excitation
- S-parameter symmetry options to decrease the solution time for many structures.
- Calculation of various electromagnetic quantities such as electric fields, magnetic fields, surface currents and power flows, current densities, power loss densities, electric energy densities, magnetic energy densities, voltages in the time and frequency domains.

- Antennas farfield calculation (including gains, beam direction, side lobe suppression, and the like) with and without farfield approximation; farfield probes to determine broadband farfield data at certain angles.
- Simultaneous port excitation with different excitation signals for each port.
- User defined excitation signals and a signal database.

#### 3.3.3.2 Eigen-Mode solver

- Calculation of modal field distributions in closed, loss-free or lossy structures.
- Adaptive mesh refinement in 3-D
- Calculation of losses and q-factors from each mode (direct or by using a perturbation method)
- Automatic parameter studies using the built in parameter sweep tool.
- Automatic structure optimization for arbitrary goals using the built in optimizer.

#### 3.3.3.3 Modal Analysis solver

- Broadband calculation of S-parameters from the modal field distributions, calculated using the Eigen mode solver.
- Re-normalization of S-parameters for specified port impedances.
- Calculation of losses and Q-factors for each mode (perturbation method)
- Automatic parameter studies by using the built in parameter sweep tool.
- Automatic structure optimization for arbitrary goals by using the build in optimizer.

#### 3.3.3.4 Frequency Domain solver

- Efficient calculation for loss-free and lossy structures including lossy wave guide ports.
- Automatic fast broadband adaptive frequency sweep
- User defined frequency sweeps
- Port mode calculation by a 2-D Eigen-mode solver in the frequency domain.
- High performance radiating/absorbing boundary conditions
- Periodic boundary conditions including the phase shift or scan angle
- Antenna farfield calculations (including gain, beam direction, side-lobe suppression, and the like) with and without farfield approximation.
- RCS calculations
- Calculation of SAR distributions
- Discrete elements as ports

#### 3.3.4 Visualization and Secondary Results Calculation

- The results can be viewed immediately during the simulations.
- Importation and visualization of external x-y data
- Various field visualization options in 2-D and 3-D for electric fields, magnetic fields power flows, surface currents and the like,
- Animation of field distributions.
- The results are easy to export and also can be easily plotted.

- Hierarchical result templates for automated extraction and visualization of arbitrary results from various simulation runs. This data can also be used for the definition of optimization goals.

A strongly interactive interface will help one to quickly achieve the desired insight into a selected device. The last, but not the least outstanding feature of the full parameterization of the structure modeler, is that which enables the use of variables in the definition of the selected device. In combination with the built-in optimizer and parameter sweep tools, the CST Microwave Studio is capable of both the analysis and design of electromagnetic devices and hence can solve virtually any high-frequency field problem.

## **Chapter 4** OPTIMIZATION OF THE PERFORMANCE OF PHOTODETECTOR

### 4.1 Introduction

In Chapters II and III, it was shown that photodetectors are an important part of an optical communications system. The role of optical receivers to convert the optical signal back into electrical form and recover the data transmitted through the light wave system was also discussed in earlier chapters. The receiver's key component is a photodetector that converts the optical signal into an electrical signal. As discussed in the previous chapters, a photodetector should have high sensitivity, fast response, low noise, low cost, and high reliability. Also, its size should be compatible with the fiber-core size. These requirements are best met by photodetectors made using semiconductor waveguides. Semiconductor photodetectors utilize the internal photoemission of electrons inside a semiconductor material and satisfy the above mentioned compatibility issues best among all other detectors.

In semiconductor detectors, photons from an incident optical signal having an energy equal to or larger than the bandgap energy are absorbed, and electrons are excited from the valence to the conduction band. The responsivity of a photodetector is the ratio of the photocurrent to the absorbed optical energy, which depends on the absorbing optical spectrum of the semiconducting material. For high responsivity the absorbing material used should have a bandgap very near, but above the upper wavelength limit of the optical signal. Improvement in quantum efficiency of

photodetectors is perhaps a key factor in improving a detectors performance. The quantum efficiency of a photodetector is defined as the ratio of electron generation rate to photon incidence rate

$$QE[\%] = \frac{1.24 \times 10^5 [Amps / Watts]}{\lambda[nm]}$$

Effects stemming from the absorption wavelength in bulk semiconductors and from diffraction drastically reduce the absorption efficiency in semiconductor light-sensing structures. Therefore, conventional photodetectors (p-i-n photodiodes, metal-semiconductor-metal [MSM] photodetectors, and others) are subject to a tradeoff between speed and quantum efficiency. In these devices, cut-off frequencies greater than 300 GHz have always been obtained with low-temperature-grown gallium arsenide (GaAs) layers. The quantum efficiency is intrinsically limited by non-radiative recombination of photo-generated carriers and is about 10% in best cases. Despite there being no significant improvement in the bandwidth-efficiency product in the last decade, high-speed and efficient photodetectors are still of considerable interest for high-speed optical communications and terahertz generation by photo-mixing. The achievement of quantum efficiencies greater than 50% with cut-off frequencies above 300 GHz requires new solutions to efficiently confine the absorption in nanoscale low-capacitance structures [22].

Conventional MSM photodetectors are made of interdigitated electrodes deposited on a bulk absorbent semiconductor. High-speed MSM structures can be obtained by decreasing the finger spacing, but their efficiency drops dramatically because of the opacity of metal electrodes. The interaction of light with the gratings of MSM

photodetectors is commonly described in geometrical terms (the light is reflected by metallic electrodes and transmitted between them); however, this explanation does not make sense for sub wavelength gratings. The grating acts as a high-reflectivity mirror for both polarizations, leading to an efficient coupling of the incident light with the cavity and an absorption efficiency of close to 100%. The MSM structure analyzed in this research effort is based on nanoscale gratings, which help to confine light and collect photo-carriers. As a consequence, there are now no limitations stemming from the absorption wavelength of the semiconductor and the opacity of the metallic electrodes.

Analyses of such detectors are possible through two different methods. First, they can be carried out using semiconductor device simulation codes (software) that would compare the collected charge with and without the gratings. The optical coupling in the detector's active region is a complex function of the angle of incidence, the wavelength of the incident light, the film thickness, and boundary conditions. For semiconductor based simulation studies, a simulated device is constructed with the same dimensions as the original fabricated device. Besides solving the basic semiconductor device relations such as Poisson's equation, and continuity and carrier transport equations, standard models for carrier recombination, lifetime, field dependent mobility and the like, as well as the optical intensity profile within the semiconductor structure are also calculated in simulations. The intensity profile is converted into the photo-generation rate at different grid points in the active detector region. The photo-induced carrier generation is the integration of the generation rate

formula over the area of intersection between the incident ray and the polygon associated with the grid point. The generation rate, G is defined as

$$G = \eta_0 \frac{P' \lambda}{hc} \alpha e^{-\alpha y} \quad (4.1)$$

where  $P'$  contains the cumulative effect of reflection, transmission and the loss due to absorption over the ray path measured in Watts per meter<sup>2</sup> and  $\frac{P'}{hc}$  is photon flux (per unit area per second),  $\eta_0$  is the internal quantum efficiency, which represents the number of carrier pairs generated per photon absorbed,  $y$  is the relative distance of the ray from the source,  $h$  is Plank's constant,  $\lambda$  is the wavelength and,  $c$  is the speed of light. The factor  $\alpha$  is expressed as

$$\alpha = \frac{4\pi}{\lambda} k \quad (4.2)$$

Where,  $\alpha$  is the absorption coefficient,  $\lambda$  is the wavelength and  $k$  is the imaginary part of the optical index of refraction and  $n$  is the real part, so that,

$$\tilde{n}(\lambda) = n(\lambda) + i \cdot k(\lambda). \quad (4.3)$$

Semiconductor based simulation, however, was not chosen as an option in this study. This is principally because device codes (software) cannot account for the influences of the grating geometry and shapes on the surface of the active region and its contribution to the overall collection mechanism. Furthermore, it would be difficult to separate the carriers generated in the grating itself from those generated in the active region that would contribute to charge collection process. The contribution from the grating would be a different problem than what this study is aimed at.

The transmission of electromagnetic signals through the gratings and the effects of the grating shape on the transmission energy is therefore a better option. Therefore, this option was followed in this study. Rigorous electromagnetic calculations of the whole structure are based on a modal method, and experiments (simulations) are carried out on Si-based substrates. If the results presented are conclusive, then the concept of increasing the transmission energy by allowing the electromagnetic waves to pass through different grating structures can be used to design such structures with optimum charge collection efficiency. Kranthi et al [27] have shown that transmitted energy into the substrate can increase by using wall like structure on the surface of the active region [27]. A detailed analysis is given in [27] and is briefly reproduced here. Consider the structure shown in Fig. 7 with a wall-like structure, on the active region:. Consider a plane wave passing through the structure into the active region as shown. The ratio of the transmitted amplitude to the incident wave amplitude is defined as the transmission coefficient. The energy transmitted into the active region is a multiple of the transmission coefficient. Thus, a higher transmission coefficient with the gratings as compared to the case without gratings can translate to more energy being transmitted to the substrate (active) region from the grating region. A higher energy transmission for the wall like grating structure as compared to a detector without the gratings is possible, as was reported in experiments. This can be explained as follows:

Since  $\tau = \frac{E_o^t}{E_o^i}$ , an increase in the transmitted wave amplitude means an increase in the

transmission coefficient. Now, consider two regions ( the grating wall as region 1 and

an active area as region 2) of the detector as shown in Fig.7 .Assuming normal incidence from region 1 into region 2, the energy carried by the wave is distributed between the reflected and transmitted wave and can be characterized in terms of the incident E field amplitude, the reflection and transmission coefficients, and the impedance of the two media( i.e. Si and air in this case). The amplitude of the transmitted E-field can be explained in terms of conservation of the time averaged power (in watts) due to the E and H fields that are crossing a given surface area A in the direction of propagation.

Starting from Eq. (3.56)

$$P = \int_A \langle S \rangle \cdot dA = S \cdot A$$

Where,  $\langle S \rangle$  is the average Poynting vector (watts/m<sup>2</sup>) derived from the instantaneous vector  $\vec{S}$  given by

$$\vec{S} = \vec{E} \times \vec{H} \tag{4.4}$$

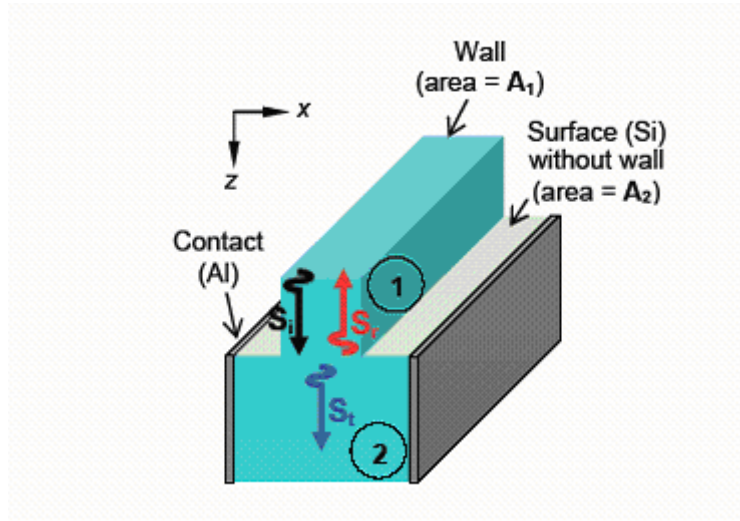


**Figure 7 Single wall grating used on the active region used for analysis**

When the wave is traveling from a region of cross sectional area  $A_1$  into a region of area  $A_2$ , one can write the relationship between the incident, reflected and transmitted waves, as

$$\langle P \rangle_1 = \langle S \rangle_i A_1 - \langle S \rangle_r A_1$$

and (4.5)

$$\langle P \rangle_2 = \langle S \rangle_t A_2$$

Hence at the interface, one can write.

$$\langle S \rangle_i - \langle S \rangle_r = \langle S \rangle_t$$

$$\frac{\langle P \rangle_i}{A_1} - |\Gamma|^2 \frac{\langle P \rangle_i}{A_1} = \frac{\eta_1}{\eta_2} |\tau|^2 \frac{\langle P \rangle_i}{A_2} \quad (4.6)$$

$$\frac{\frac{\eta_1}{\eta_2} |\tau|^2}{1 - |\Gamma|^2} = \frac{\frac{\eta_1}{\eta_2} |\tau|^2}{1 - |\tau - 1|^2} = \frac{A_2}{A_1}$$

If the material in region 1 is the same as in region 2 ( $\eta_1 = \eta_2$ ), and if it is assumed that  $A_2 > A_1$ , it follows from Eq. (4.6) that  $\tau > 1$ . Thus, the amplitude of the transmitted wave is greater than the amplitude of the incident wave, and an increase in  $\tau$  (where  $\tau = \frac{E_o^t}{E_o^i}$ ) also translates to more energy deposition in the transmission or active region of the detector.

With more energy available than before due to the presence of gratings on the surface, the wall-like structure contributes to the production of a larger number of electron-hole pairs in the active region, as compared to an MSM detector without the wall-like grating structure. It is therefore of interest to determine whether the wall or any other geometry such as a square, cone or any other shape would contribute to more energy being in the active region and consequently improve the charge collection efficiency of the detector.

Thus, the objective of this thesis is two-fold. The first part is to determine which grating shape will lead to maximum energy in the substrate, and once this is determined, then optimize the contribution from that structural shape. In this thesis an EM field transport process is further studied with a detailed analysis of the structure and geometry necessary for maximum energy deposition in the active region. In particular, an attempt to optimize the collection efficiency by optimizing the grating shape, height and the area covered by the gratings on the active region is made. Variations in the amplitude of the transmitted electric field intensity of the photodetector were determined for each case in order to ensure the maximum possible

collection efficiency. Finally, this chapter also analyzes the effects of a coating over these grating structures by examining the variations in the electric field in the substrate (active region).

## 4.2 Comparison between Different Structures

In the simulations, a bulk Si slab of dimensions  $10 \times 10 \times 2 \mu\text{m}$  was used as the substrate for an MSM photodetector as shown in Fig 9.a. A 1-V/m plane wave port as the source in the negative  $y$ -direction as a continuous sinusoidal wave was used as the excitation signal Fig 8. For Si, it is also important that the incident wave has energy equal to or greater than the material bandgap and hence is capable of creating electron-hole pairs at the interface.

A wavelength corresponding to the bandgap energy was therefore chosen for the simulations. In order to optimize the E-fields, different grating shapes, i.e. square, cone and hatched cone, as shown in Figs. 9b, 9c, and 9d, respectively were tried. E-fields were computed by placing the probes at the interface between two regions (gratings and the Si substrate) as the electromagnetic pulse traveled through the grating and into the active region.

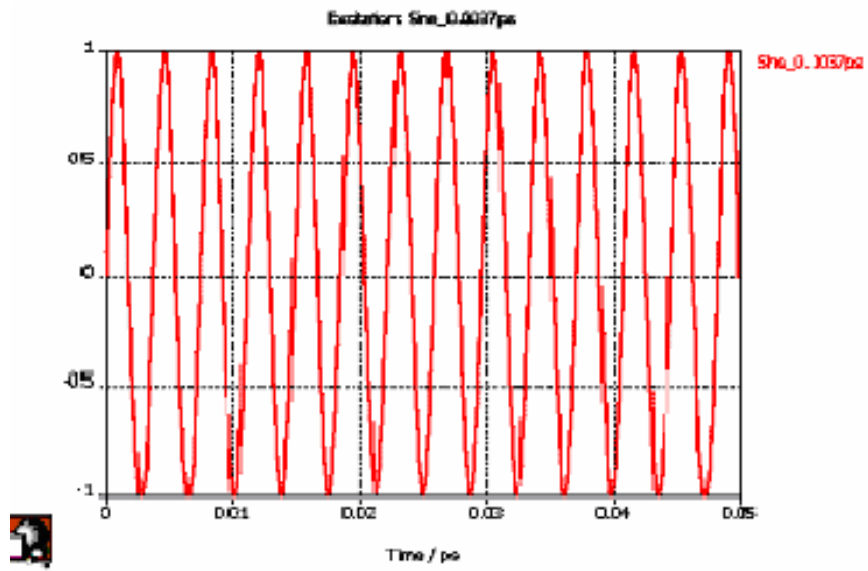


Figure 8 Input Excitation Signal (continuous sine wave)

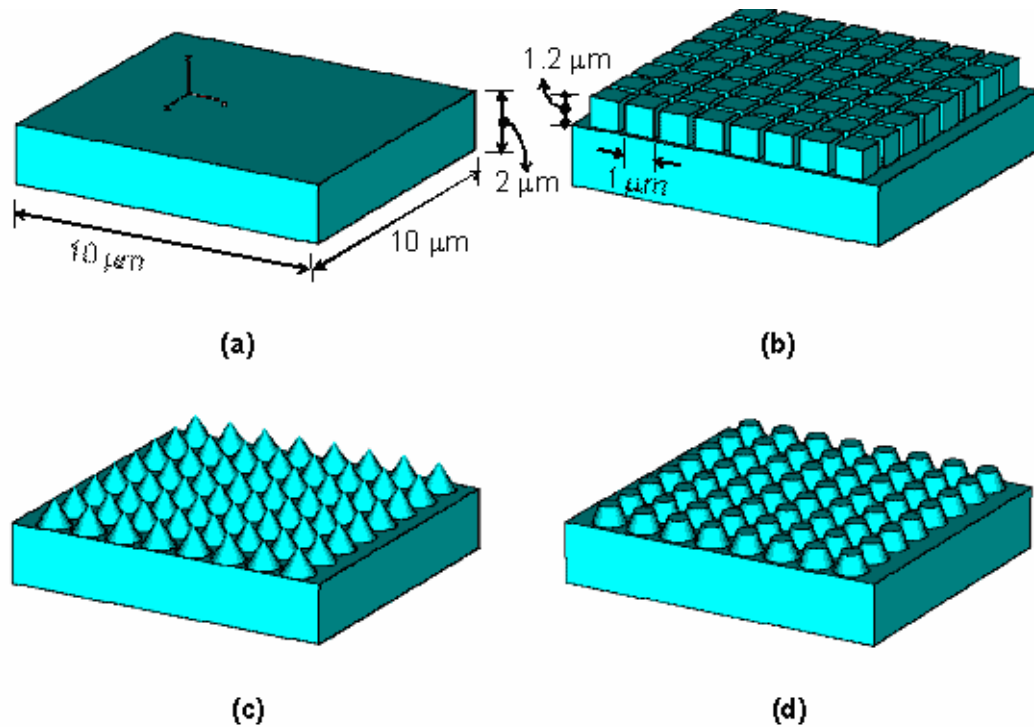
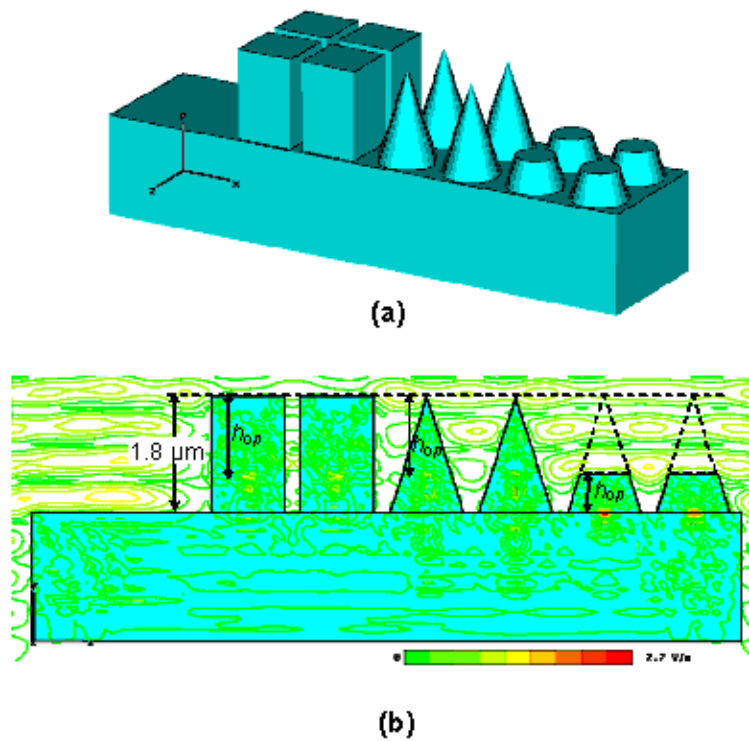


Figure 9 Configuration of MSM photodetectors used in simulation. Structures are a  $10 \times 10 \times 2 \mu\text{m}$  Si-substrates (a) without gratings (b) square gratings (c) cone gratings (d) hatched gratings

As shown Figs 10 and 11, the hatched cone structure has the maximum E-field among the three structures. Fig 10 shows the cross-sectional view of all three shapes and also

the case without any gratings. It is seen that energy transmitted to the substrate is much less when there is no grating compared to when there is a grating. Also, Fig 11 it shows the top view of the three structures, and it also shows that the hatched cone has the maximum intensity at the center in the form of a circle.

Fig 10 & 11 are plotted in the time-domain. In Fig 11 it is seen that the hatched cone and the cone show a circular pattern and in the case of a square, there are four spots. This pattern formation is because the gratings on the substrate behave as a waveguide. Therefore it takes the patterns at different modes as TEM waves.



**Figure 10 (a) Bulk Si photodetector with different 1.8-μm tall grating structures i.e square, cone and hatched cone (b) isoline plot of incident wave transmitted through substrate, square, cone and hatched cone structures. The curves display the optimum height,  $h_{op}$  of each structure**

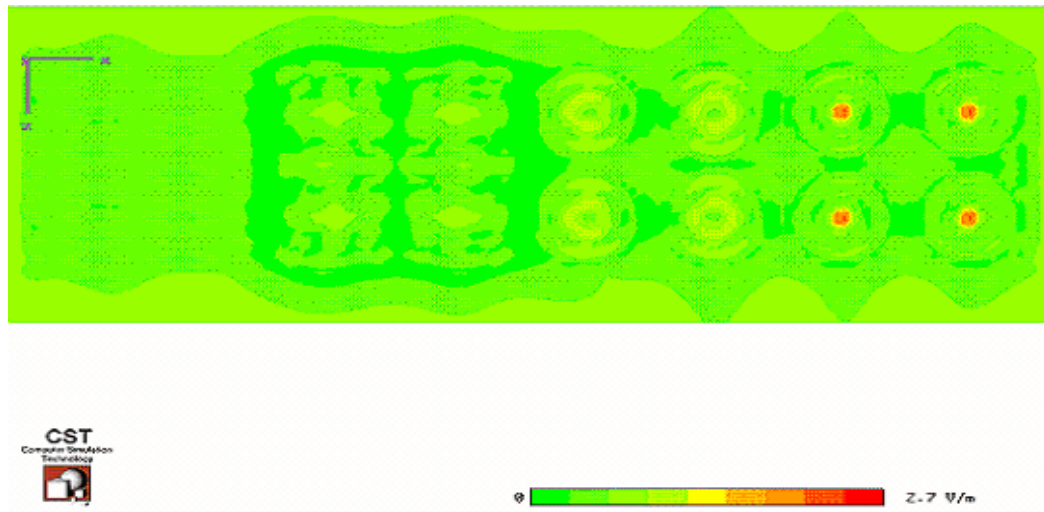


**Figure 11 Top view of a contour plot of the incident wave transmitted through the substrate: square, cone, and hatched cone structures**

From the above discussion, the hatched cone-cut has the best results among the three structures. The hatched cone has a flat top as a square grating and has comparatively less leakage than a cone grating. Therefore, most of the energy is transmitted to the active region and gives the best results

#### 4.3 Optimization by varying the height of gratings

In order to improve the efficiency further, the structures shown in Fig 9a were simulated by varying the height of the gratings from 0.5-1.3  $\mu\text{m}$ , while the area covered on the active region was kept the same for all the structures. A device with 64 square gratings as shown in the Fig.12 was simulated, while the height of each grating was varied from 0.5-1.3  $\mu\text{m}$ . As the height is increased from 0.5 $\mu\text{m}$  to 1.3 $\mu\text{m}$ , the E-field initially increased up to a certain critical height and then, started to

decrease as the height was increased further. Fig.12 shows that square gratings have an optimum E-field of 1.84V/m at a height of 1 $\mu$ m.

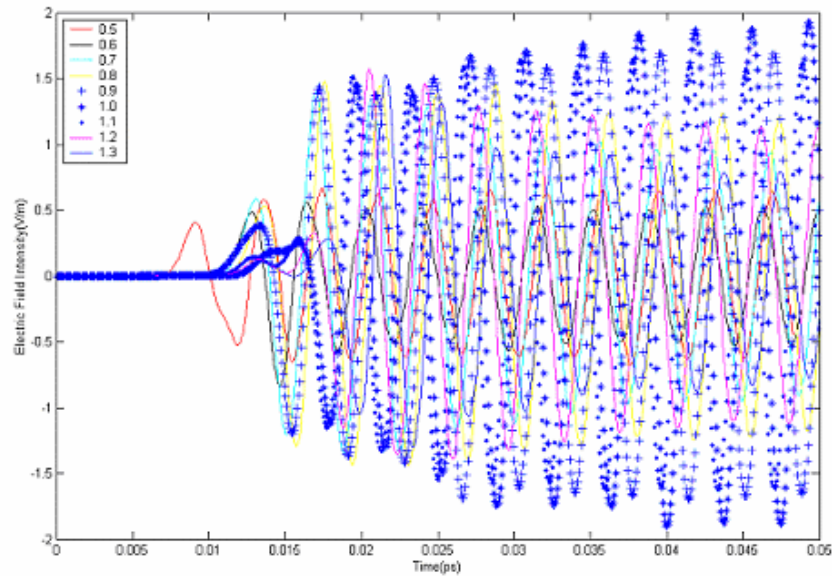


**Figure 12 Incident wave amplitude change for a square grating with the grating height varying from 0.5 $\mu$ m to 1.3 $\mu$ m**

The simulation results for device with cone gratings as shown in Fig 13 were obtained by varying the height of each grating from 0.5-1.3 $\mu$ m. From the figure, it is seen that an optimum E-field of 1.55V/m at a height of 0.9 $\mu$ m was achieved. The decrease in the E-field amplitude with an increase in the height of the cone beyond the critical point is due to the change in the angle of the cone with the base. With an increase in the height, the cone becomes increasingly steep, and the energy transmitted through the cone has a less chance of reaching the substrate, since there is a greater chance for leakage through a steeper cone.

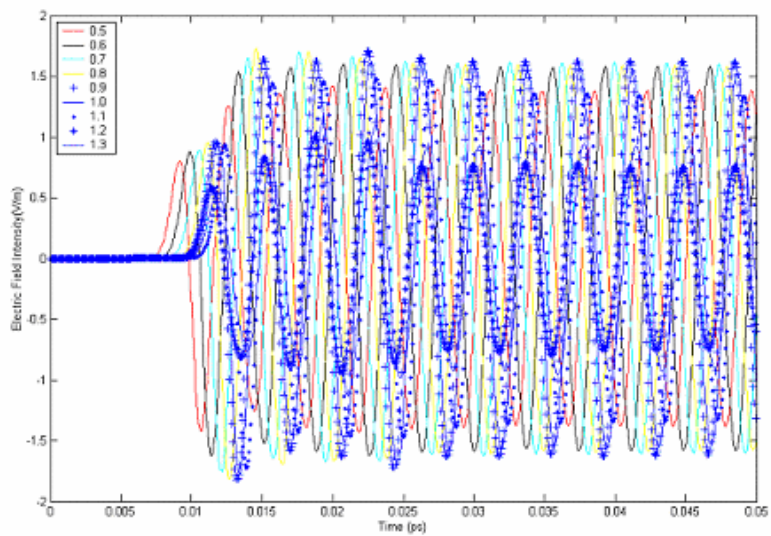


**Figure 13 Incident wave amplitude change for a cone grating with the grating height varying from 0.5 $\mu\text{m}$  to 1.3 $\mu\text{m}$**

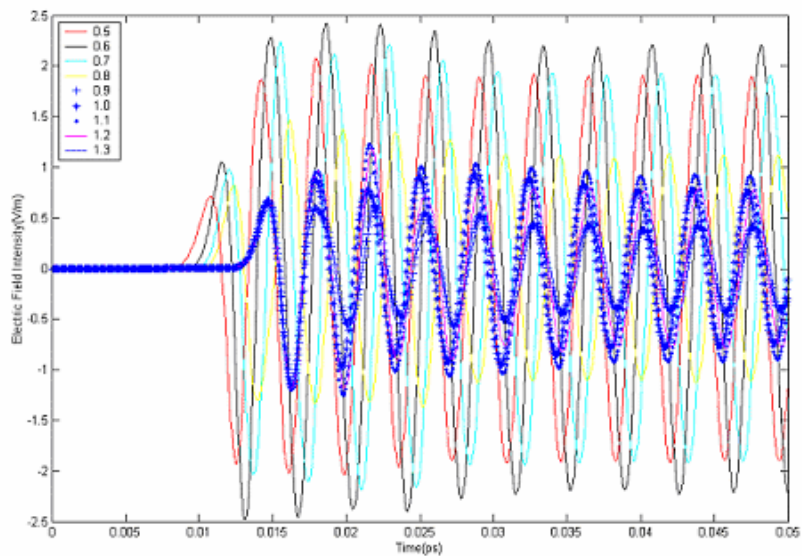


**Figure 14 Incident wave amplitude change for a hatched cone grating with the grating height varying from 0.5 $\mu\text{m}$  to 1.3 $\mu\text{m}$**

In Fig. 14 for the hatched cone with the grating height varying from 0.5-1.3 $\mu\text{m}$ , an optimum E-Field at a height of 0.6 $\mu\text{m}$  is achieved. The plots of normalized E-field amplitudes associated with the square, cone, and hatched cone structures with different heights are shown in Fig. 15 for comparison. As discussed earlier, each structure has a unique optimum height,  $h_{op}$ , with the square, cone, and hatched cone having optimum heights of 1.0  $\mu\text{m}$ , 0.9  $\mu\text{m}$ , and 0.6  $\mu\text{m}$ , respectively. The hatched cone structure of Fig. 9d shows a maximum normalized amplitude of 2.45 V/m at a height of 0.6  $\mu\text{m}$  as seen in Fig. 15 This allows for maximum energy transfer into the substrate. The fabrication cost is also expected to be the least due to its low height,  $h_{op}$ . The reason for the high transmitted amplitude for the hatched cone as compared to the other two structures could be a combination of the effects of a slant-side and flat-top surfaces that result in focusing the transmitted waves on one particular spot close to the top surface. As a result, the hatched cone structure offers high magnitude E-fields. In Fig 10 an isoline plot of the three shapes is shown; here it is shown that the hatched cone has the highest E-field and also it is close to the active region. In the cases of the square and the cone, the focus point is not so close to the active region. Also, as the height is increased, the focus point shifted slightly towards the top and thus there is a decrease in the E-field in all the three grating structures.

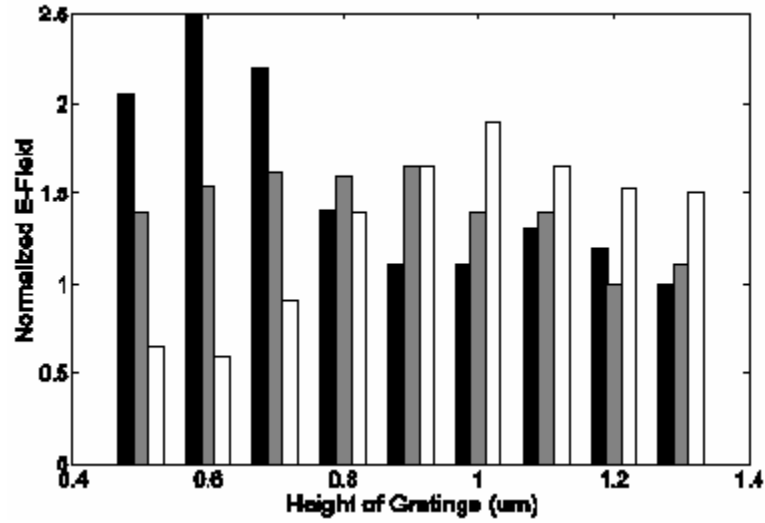
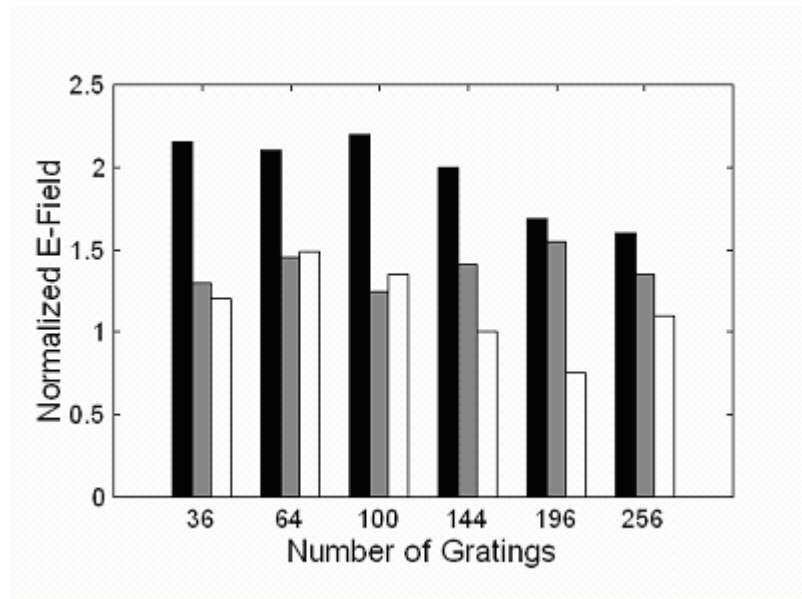


Figure 15 Normalized (with 1 V/m) E-field peak associated with a square (white), cone (gray), and hatched cone (black) structures as a function of height.

#### 4.4 Optimization by Varying the Number of Gratings on the Active Region

In order to optimize the charge collection efficiency, the number of grating structures on the active region was varied. By doing this, one is actually changing the area covered by the gratings, keeping the area of the active region constant, so that one is changing the percentage of the area covered by the Si gratings on the active region. The dimension of the substrate is kept constant while the area on the active region covered by the gratings is changed by changing the number of gratings. The dimension of each grating structure is kept constant at  $a \mu\text{m}^2$ , where  $a$  is the area covered by each grating structure on the active region. Hence, the entire area covered by the grating is  $na \mu\text{m}^2$  ( $n$  = number of gratings). The relationship between the number of gratings and the normalized E-field is shown in Fig. 16 for all three grating structures. One can see that the highest E-field corresponds to  $n=64$  for the square,  $n=196$  for the cone and  $n=100$  for the hatched cone

gratings. The E-field magnitude starts at a low level with fewer gratings and then slowly increases until a certain critical number of gratings are reached before beginning to reduce. It is been proved that charge collection efficiency can be increased by structuring the surface region of the semiconductor material using physical optic scales smaller than a wavelength [26]. In the current study here, when the number of gratings  $n$  is 36, the distance between the gratings is larger than the wavelength. As the number of gratings increases, the distance between the gratings becomes less than the wavelength, causing the E-field magnitude to increase. The E-field then starts to decrease when the number of gratings further increases beyond a critical number ( $n = 100$  in case of hatched cone). The reason is that, even though the physical scale is less than the wavelength, a large number of spikes cause the E-field behavior to approach that of toward a bulk Si substrate.



**Figure 16 Relationship between the number of gratings and the normalized E-field peak associated with square (white), cone (gray), and hatched cone (black) structures as a function of height.**

#### 4.5 Optimization of Charge Collection Efficiency by Using a Cladding of SiO<sub>2</sub>

In the above two cases, the hatched cone had the highest E-field. In further attempts to improve the charge collection efficiency, a cladding was used on the device because it would prevent leakage of the charges especially for the higher power transmission into the active region, thereby enhancing the collection efficiency due to the back reflections from the surface. In order to do this a material with a refractive index less than Si should be used; therefore SiO<sub>2</sub> was used.

In this case, the Si substrate with a dimension of 10×10×2 μm is shown in Fig. 17. The Si gratings with optimum height have been used in this case. The gratings have been coated with a SiO<sub>2</sub> layer of thickness 0.1 μm. The E-field probe was placed at the interface between the Si and the gratings, as the wave first falls on the Si gratings. Varying the height of the Si and SiO<sub>2</sub> coating by +0.1 and -0.1 μm of the optimum height of the grating, the plots are shown in Fig. 18. There is a slight improvement in the E-field with the cladding structure as compared to the grating without cladding. The increase in the E-field could be due to the back reflections inside the grating structures.

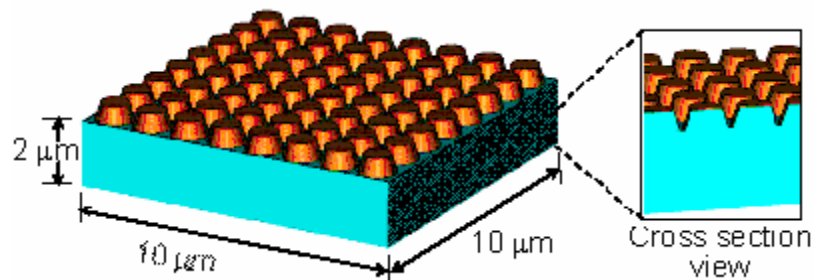


**Figure 17 Structure consists of a 10×10×2 μm Si substrate. The Si hatched cone gratings on top of the bulk Si are coated with a SiO<sub>2</sub> layer of thickness 0.1 μm**

In case of the hatched cone, the maximum E-field was attained at the optimum height as shown in Fig 18. Similarly, the square and the cone gratings with coatings also have maximum E-field at an optimum height as shown Figs 20 and 22.

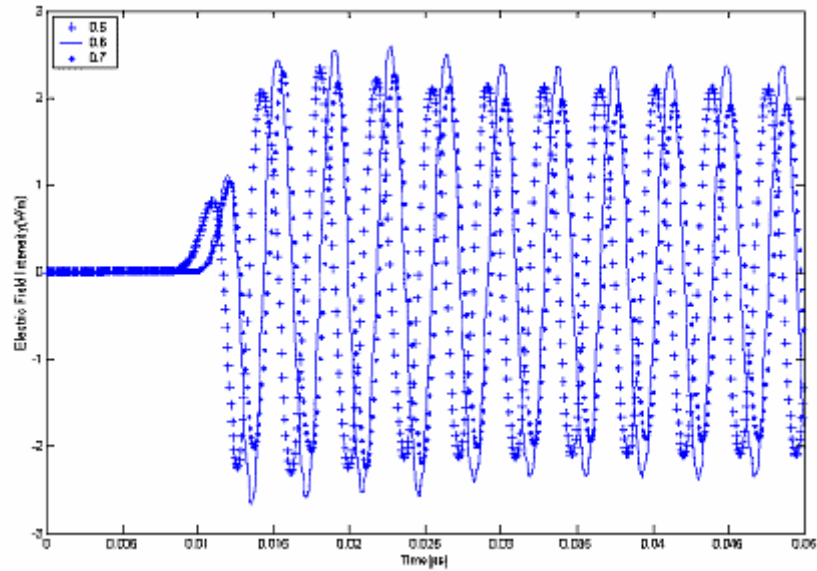


**Figure 18** Waveforms of E-fields of the structure consisting of hatched cone Si and SiO<sub>2</sub> coating with different heights (+: 0.5 $\mu\text{m}$ , line: 0.6 $\mu\text{m}$ , and \*: 0.7 $\mu\text{m}$ )

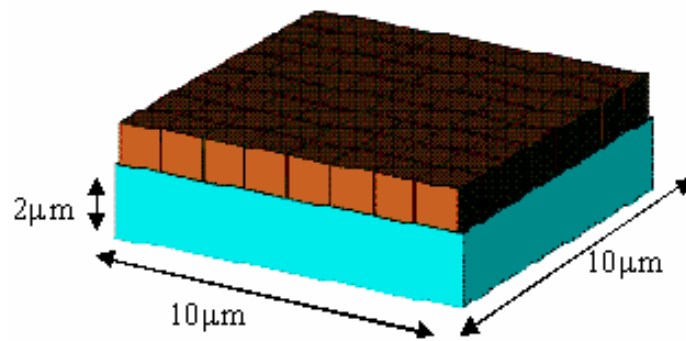


**Figure 19** Structure consists of a 10 $\times$ 10 $\times$ 2  $\mu\text{m}$  Si substrate. The Si square gratings on top of the bulk Si are coated with SiO<sub>2</sub> layer of thickness 0.1 $\mu\text{m}$

The hatched cone has the maximum E-field with a cladding. A SiO<sub>2</sub> cladding is used in the here analysis as the oxide layer to limit the Si thickness and thus improve the speed of the detector. Also, because the SiO<sub>2</sub> refractive index is less than that of Si, most of the incident wave on the gratings is reflected back into the detector. Large amounts of energy are deposited on the detector's active region, leading to an increase in the charge collection efficiency of the photodetector.

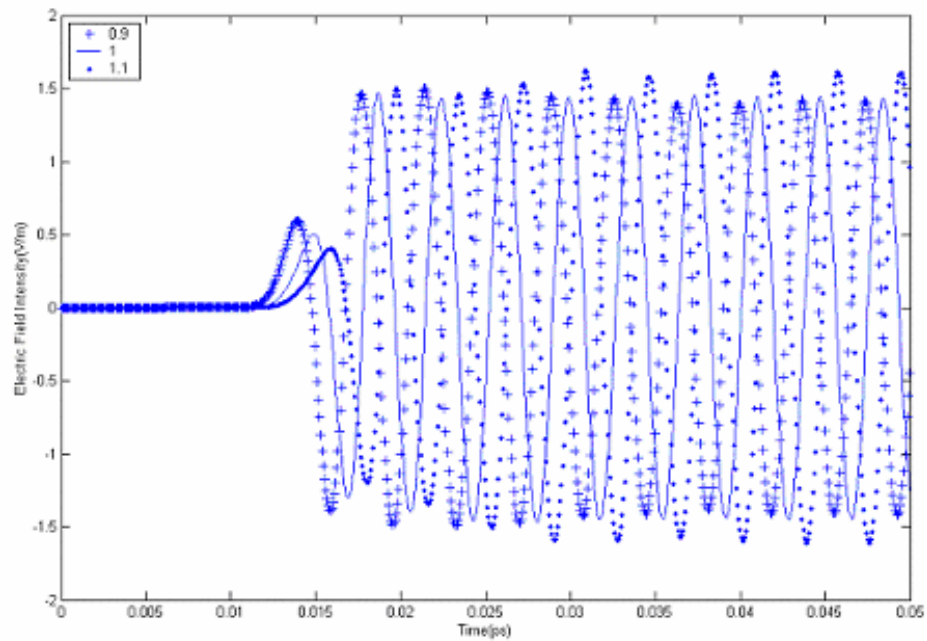


**Figure 20 Waveforms of E-fields of the structure consisting of square Si and an SiO<sub>2</sub> coating with different heights (+: 0.5 $\mu$ m, line: 0.6 $\mu$ m, and \*: 0.7 $\mu$ m)**

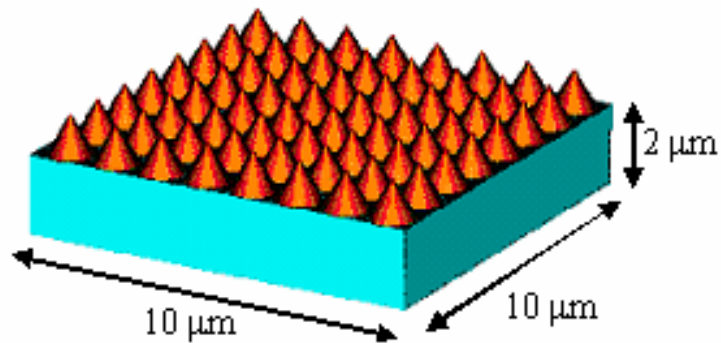


**Figure 21** Structure consists of a  $10 \times 10 \times 2 \mu\text{m}$  Si substrate. The Si cone gratings on top of the bulk Si are coated with  $\text{SiO}_2$  layer of thickness  $0.1 \mu\text{m}$

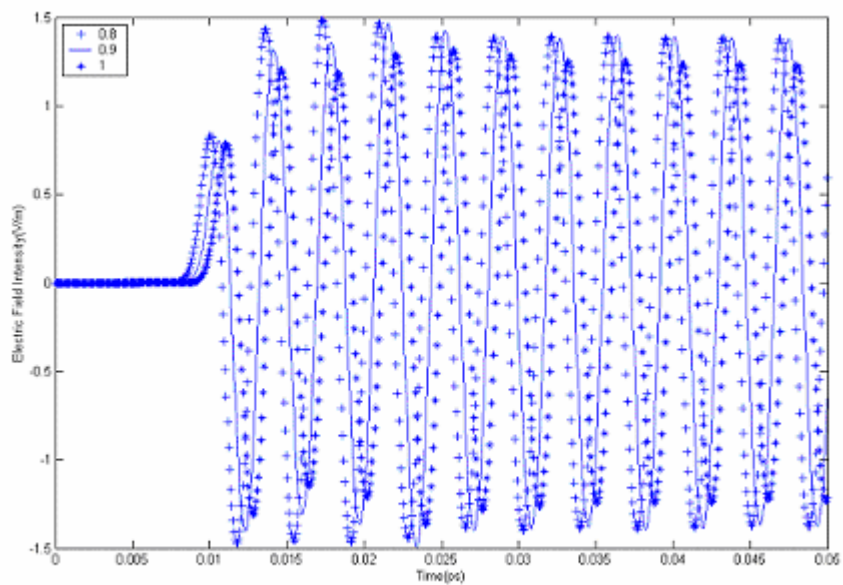


**Figure 22** Waveforms of E-fields of the structure consisting of cone Si and  $\text{SiO}_2$  coating with different heights (+:  $0.5 \mu\text{m}$ , line:  $0.6 \mu\text{m}$ , and \*:  $0.7 \mu\text{m}$ )

Because the hatched cone gave the best results for of the all above cases, the hatched cone is used in the following discussion. In order to optimize the device performance,

the dimensions of the Si substrate are changed to  $10 \times 10 \times 4 \mu\text{m}$  and a layer of cladding is added to the substrate as shown in Fig 23.

Initially, a layer of  $\text{SiO}_2$  of dimensions  $10 \times 10 \times 4 \mu\text{m}$ , which has a low refractive index than Si, was used and the results were simulated. Fig 24 shows that there is an improvement by adding the  $\text{SiO}_2$  layer on top of the Si substrate.

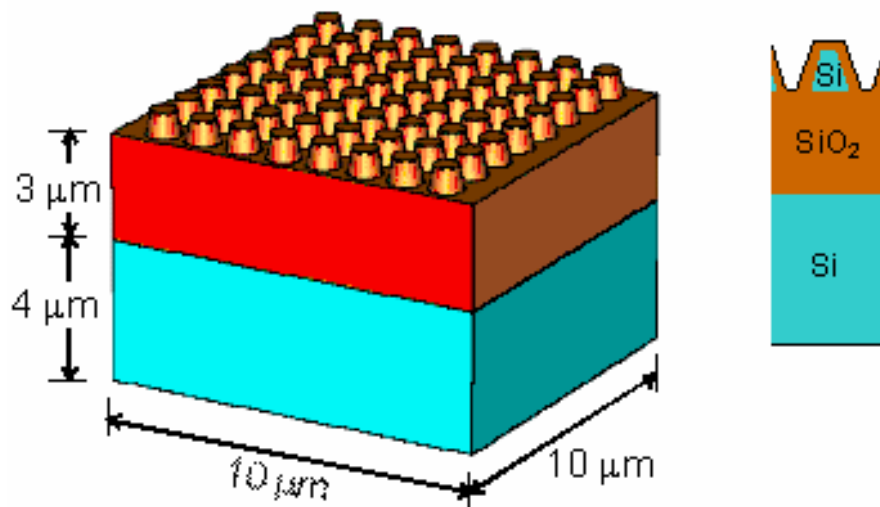


**Figure 23** Structure consists of a  $10 \times 10 \times 4 \mu\text{m}$  Si substrate with a bulk cladding layer of  $\text{SiO}_2$  added on top of Si layer with a dimension of  $10 \times 10 \times 3 \mu\text{m}$ . The Si hatched cone gratings on top of the bulk  $\text{SiO}_2$  are coated with a  $\text{SiO}_2$  layer of thicknesses  $0.1 \mu\text{m}$

The reason for this improvement could be, because the dielectric constant of the material is dependent on the plasma frequency as shown below Eq 4.3, and if the incident frequency is less than the plasma frequency, the material behaves as a transparent material and reaches the substrate directly; otherwise the incident waves interacts with the cladding layer.

From Chapter 3, consider the wave equation

$$\nabla^2 E = \frac{\varepsilon}{c^2} \frac{\partial^2 E}{\partial t^2} \quad (4.7)$$

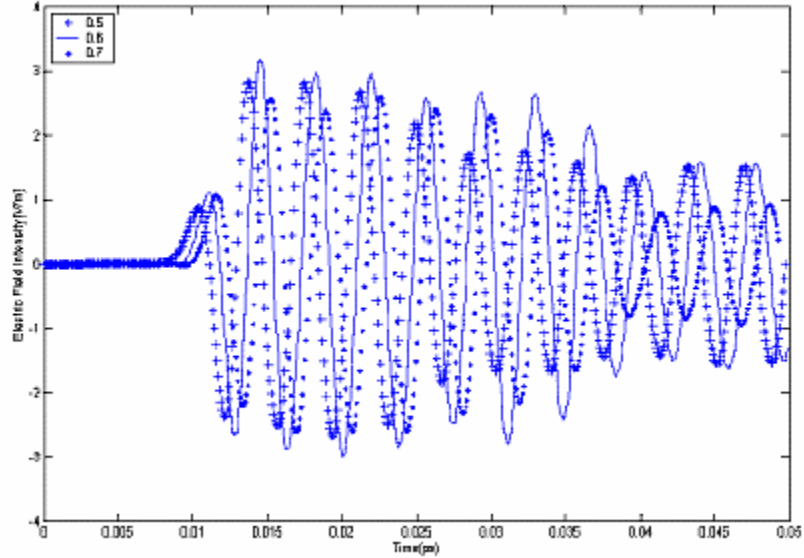


Figure 24 Waveforms of E-fields of the structure consisting of hatched cone Si and SiO<sub>2</sub> coating and a bulk cladding layer on the substrate with different heights (+: 0.5 μm, line: 0.6 μm, and \*: 0.7 μm).

A plane wave solution to the wave equation is given as

$$E(r, t) = E_0 e^{i(k \cdot r - \omega t)} \quad (4.8)$$

where  $E_0$  is the electric field amplitude,  $k$  is the wave vector, and  $\omega$  is the frequency.

Substituting Eq 4.8 into Eq 4.7 yields the following condition

$$c^2 k^2 = \omega^2 \varepsilon(\omega) \quad (4.9)$$

Another material with a different refractive index that is less than the refractive index of Si can be used as a cladding layer to improve the performance. From the above

discussion, the hatched cone with a SiO<sub>2</sub> coating on the Si gratings and a SiO<sub>2</sub> layer on the bulk substrate give the best results.

## Chapter 5 CONCLUSION AND FUTURE WORK

In this research, the main aim was to optimize the charge collection efficiency of a silicon MSM photodetector that has gratings on the surface of the active region. The submicron gratings of different shapes were studied through an electromagnetic simulation code (software). Wave transmission through the various grating structures were studied to determine which shape allowed for the maximum energy transmission through it and into the substrate, which is the active region. Grating shapes such as a square, a cone, and a hatched cone were used in order to optimize the charge collection efficiency of the device.

Plots of the electric field amplitude as it propagates from the constricted grating region to a larger cross-section in the active region were analyzed for comparison. The height of each grating was varied from 0.5-1.3 $\mu\text{m}$ . It was found that the hatched cone had the maximum E-field of 2.45V/m at a height of 0.6 $\mu\text{m}$ . The square had a maximum E-field at an optimum height of 1 $\mu\text{m}$  and the cone at 0.9 $\mu\text{m}$ . The hatch-top cone gave the maximum E-field followed by the square and the cone gratings. This study shows that a cone shaped structure with a hatched-top allows for maximum energy transfer into the active region, thus enhancing the collection efficiency. The height required for maximum energy transfer for the hatch-cone is also a minimum, as compared to a full cone or a square shaped grating.

The hatched cone seems to be the best structure since it combines the advantage of a square and a cone shape allowing the EM waves to concentrate at a point closer to the active region giving rise to higher energy transmission. Also, the hatched cone has the least height compared to the other structures; as a result, the fabrication costs would be less in this case.

Isoline and contour plots of all the three structures were also presented for comparison. The cross sectional and top view of the device showed a maximum intensity in case of the hatched cone. The higher transmitted amplitude for the hatched cone as compared to the other two structures could be due to a combination of the effects of slanted sides and flat-top surfaces that result in focusing the transmitted waves on one particular spot close to the top surface. As a result, the hatched cone structure has high E-fields.

In order to determine whether the area covered by the gratings on the active region of each grating would affect the device performance, simulations were performed by increasing the number of gratings on the active region surface while keeping the height of the gratings and the area of the active region constant. Square gratings had a maximum E-field at 64 gratings, the cone at 196 gratings and the hatched cone at 100 gratings. The E-field of all the structures stopped increasing after reaching an optimum number of gratings after which, the E-field decreased. Also as the number of gratings was decreased, the E-field decreased when the distance between each grating was greater than the wavelength of the incident wave.

Further simulations involved the addition of cladding on the gratings while keeping the dimensions of the substrate constant. The hatched cone gave the maximum E-field again, followed by the square and the cone gratings. There was a slight improvement in the E-field of the cladding structure as compared to gratings without cladding. A cladding of SiO<sub>2</sub> was used on all the gratings; a SiO<sub>2</sub> cladding was used in this analysis as the oxide layer to limit the Si thickness and thus improve the speed of the detector. The increase in the E-field could be due to the back reflections inside the gratings. A layer of another material was used directly on the substrate and it was found that the effect of layer of cladding on the substrate depends on the refractive index of the material. We found that the device with SiO<sub>2</sub> cladding layer gives the best result with hatched grating.

Charge collection efficiency of an MSM photo detector can be improved by adding gratings in the active region. Energy deposited in the active region depends on the shape and height of the gratings. This indirectly affects the charge collection efficiency of the photodetector. Also a cladding on the gratings can also be used to improve the efficiency further. Comparing the three different shapes used, it was determined that a cone shaped grating with a hatch top is the best structure for enhancing collection efficiency. Further, the hatched cone grating shape with SiO<sub>2</sub> cladding has shown the best result.

It is suggested that further studies be conducted on the charge collection efficiency of this particular MSM photodetector by using different grating shapes that are easy to fabricate. Cladding materials, in particular, needs further study to determine their

contribution in improving the collection efficiency by controlling leakages and through internal reflections. Also, the collection efficiency of the MSM photodetector needs further study by changing the EM source to a real world situation such as a horn antenna or a dipole antenna.

## REFERENCES

- [1] K. Kato, "Ultrawide-band/high-frequency photodetectors," IEEE Trans. Microwave Theory Tech, vol.47, pp1265-1281, July (1999).
- [2] R.G DeCorby, A. J.P.Hnatiw, J.N.McMullin, "Techniques to improve speed and efficiency of photodetectors", Proc. Of the IEEE Canadian conference on electrical and computer engineering, Show conference Center, Edmonton, Alberta, Canada, May9-12, (1999)
- [3] J.F.Holzman, F.E.Vermeulen, and A.Y.Elezzabi, "Ultrafast photoconductive self-switching of subpicosecond electrical pulses, "IEEE J.Quan.Electron, vol. 36, pp. 130-136, Feb (2000)
- [4] M.Caria, L. Barberini, S. Cadeddu, A. Giannattasio, A. lia, A. Rusani, A. Sesselego", Far UV responsivity of commercial silicon photodetectors", Nuclear Instruments and Methods in Physics Research A, 466, pp. 115-118 (2001).
- [5] M.Y. Liu, E. Chen, and S.Y. Chou, "140 GHZ metal0semiconductor-metal photodectors on Silicon-on-insulator substrate with scaled layer," Appl. Phys. Lett. Vol. 65, pp. 887-888, 1994
- [6] Stephane Collin, Fabrice Pardo, Roland Teissier, and Jean- Luc Pelouard, "Efficient light absorption in metal-semiconductor-metal nanostructures", Appl. Phys. Lett., vol. 85(2).July 2004.

- [7] Qing.Z. Liu, R. Ian Mac Donald, "Controlled Nonlinearity Monolithic Integrated Optoelectronic Mixing Receiver", IEEE Phot. Tech. Lett., vol.5 (12), pp/1403-1406, Dec (1993).
- [8] P.H. Shen Et al, "Interdigitated finger semiconductor photodetector for optoelectronic mixing", Proc.SPIE, vol.4028, pp.426-435, July (2000)
- [9] Y. Liu, W.Khalil, P.B. Fisher, S.Y. Chou, T.Y. Hsiang, S.Alexandrou, R. Sobolewski, " Nanoscale Ultra Metal- Semiconductor-Metal Photodetectors", 50<sup>th</sup> Annual Device Research Conference, pp 162-163, June 22-24(1992)
- [10] Sang-Woo Seo et al, "High-Speed Large- Area Inverted InGaAs Thin-Film Metal-Semiconductor-Metal Photodectors", IEEE J of Selected Topics in Quant Electronics, vol.19, no.4, July/August (2004)
- [11] M.Ghioni, F.Zappa, V.P. Kesan, and J. Warnock, "A VLSI-compatible high-speed silicon photodetector for optical data link applications", IEEE Trans Electron Devices, vol.43 (7), pp. 1054-1060, July (1996)
- [12] J.S.Wang, C.G.Shih, W.H. Chang, J.R. Middleton, P.A. Apostolakis, and M.feng, "11-GHz bandwidth optical integrated receivers using GaAs MESFET and MSM technology", IEEE Phot. Tech. Lett. Vol.5,pp.316-318,(1993)
- [13] A. Sayles and J.Uyemura, "An optoelectronic CMOS memory circuit for parallel detection and storage of optical data", vol, pp.316-318, (1993)
- [14] H.C.Lee and B.V. Zeghbroeck," A novel high-speed silicon MSM photodetector operating at 830nm wavelength", IEEE Trans. Electron. Devices, vol. 16, pp. 175-177(1995)

- [15] N.F. Mott and E.A.Davis, "Electronics Processes in Noncrystalline Materials", 2<sup>nd</sup> Ed, Oxford Univ. Press, Oxford, UK (1979)
- [16] K. Kishino, M.S. Unlu, J. I. Chyi, J. Reed, L.Arsenault, and H. Morkoc, "Resonant cavity-enhanced(RCE) photodetectors", IEEE. J. Quan. Electronics, vol. 27(8), pp. 1064-1066(1996)
- [17] Y.L. Ho and K.S.Wong, "Bandwidth enhancement in Si metal-semiconductor metal photodetectors by trench formation", IEEE. Phot. Tech. Lett, vol.8, no.8, pp.1064-1066(1996)
- [18] L.H. Laih, T.C.Chang, Y.A. Chen, W.C. Tsay and J.W.Hong, "Characteristics of MSM photodiodes with trench electrodes on p-type Si wafer", IEEE. Trans.of Electron. Devices, vol.45, pp.2018-2023(1998)
- [19] J.J.Kuta et al, "Polarization and wavelength dependence of metal-semiconductor-metal photodetector response", Appl. Phys. Lett. vol.64. no.2 Jan(1994)
- [20] Jinkwook Burm et al, "High frequency, High efficiency MSM Photodetectors", IEEE J.Quan. Electronics, vol. 31, no.8, Aug (1995)
- [21] Marta McWright Howerton, Ted E. Batchman, "A Thin-Film Waveguide Photodetector Using Hydrogenated Amorphous Silicon", J. Lightwave Technology, vol. 6, no. 12. December (1988)
- [22] Stephen. Y. Chou, Mark Y. Liu, "Nanoscale Tera-Hertz Metal-Semiconductor-Metal Photodetectors", IEEE. J. Quan Electronics, vol.28, no.10, Oct (1992)

- [23] E. Sano, "A Device model for metal-semiconductor-metal Photodetector and its application to optoelectronics integrated circuit simulation", IEEE. Trans Electron Devices, vol 37, no.9, pp1964-1968, Sep (1990)
- [24] A. K Sharma, K. A. M. Scott, S.R.J.Brueck, J.C.Zolper, D.r. Myers, "Ion Implantation Enhanced Metal-Si-Metal Photodetectors", IEEE Phot. Tech. Letter, vol.6.no. 5. May (1994)
- [25] A. K .Sharma, S. H. Zaidi, P.C. Logofu, and S. R. J. Brueck, "Optical and Electrical Properties of Nanostructured Metal-Silicon0Metal Photodetectors", IEEE. J. Quant. Electronics, vol.38, no.12, pp. 1651-1660, (2002)
- [26] A. K. Sharma, S. H. Zaidi, G. Liechty, and S. R. J. Brueck, *Proceeding of IEEE Nanotechnology*, p. 368, (2001)
- [27] Nakka S. Kranthi, "Charge collection mechanisms in a sub-micron grated photodetector: field analysis", thesis University of Missouri Columbia May (2005)
- [28] Kwak. K. Ng, "Complete guide to semiconductor devices", McGraw Hill, Inc, (1995)
- [29] Fawwaz.T.Ulaby, "Fundamentals of Applied Electromagnetics", Pearson Education Inc, (2004) Media Edition
- [30] User Manual, CST Microwave Studio 5.0 (2005)

- [31] Hari Singh Nalwa, "Photodetectors and Fiber Optics", Academic Press, (2001)
- [32] Govind.P.Agarwal, "Light wave Technology: Components and Devices", John Wiley & Sons, Inc, (2004)
- [33] Silvano Donati, "Photodetectors: Devices, Circuits, and Applications", Prentice Hall PTR, (2000)